

## SUZAKU OBSERVATIONS OF NEAR-RELATIVISTIC OUTFLOWS IN THE BAL QUASAR APM 08279+5255.

C. SAEZ,<sup>1</sup> G. CHARTAS,<sup>1</sup> AND W. N. BRANDT<sup>1</sup>

*Draft version March 16, 2009*

### ABSTRACT

We present results from three *Suzaku* observations of the  $z = 3.91$  gravitationally lensed broad absorption line quasar APM 08279+5255. We detect strong and broad absorption at rest-frame energies of  $\lesssim 2$  keV (low-energy) and 7–12 keV (high-energy). The detection of these features confirms the results of previous long-exposure (80–90 ks) *Chandra* and *XMM-Newton* observations. The low and high-energy absorption is detected in both the back-illuminated (BI) and front-illuminated (FI) *Suzaku* XIS spectra (with an *F*-test significance of  $\gtrsim 99\%$ ). We interpret the low-energy absorption as arising from a low-ionization absorber with  $\log N_{\text{H}} \sim 23$  and the high-energy absorption as due to lines arising from highly ionized ( $2.75 \lesssim \log \xi \lesssim 4.0$ ; where  $\xi$  is the ionization parameter) iron in a near-relativistic outflowing wind. Assuming this interpretation we find that the velocities in the outflow range between  $0.1c$  and  $0.6c$ . We constrain the angle between the outflow direction of the X-ray absorber and our line of sight to be  $\lesssim 36^\circ$ . We also detect likely variability of the absorption lines (at the  $\gtrsim 99.9\%$  and  $\gtrsim 98\%$  significance levels in the FI and BI spectra, respectively) with a rest-frame time scale of  $\sim 1$  month. Assuming that the detected high-energy absorption features arise from Fe XXV, we estimate that the fraction of the total bolometric energy injected over the quasar's lifetime into the intergalactic medium in the form of kinetic energy to be  $\gtrsim 10\%$ .

*Subject headings:* cosmology: observations — X-rays: galaxies — galaxies: active — quasars: absorption lines

### 1. INTRODUCTION

Recent observations of nearby galaxies indicate a  $M_{\text{BH}}-\sigma$  relation (e.g., Ferrarese & Merritt 2000; Gebhardt et al. 2000), where  $M_{\text{BH}}$  is the mass of the central black hole and  $\sigma$  is the velocity dispersion of the stars in the bulge of the host galaxy. The presence of a  $M_{\text{BH}}-\sigma$  relation suggests that a feedback mechanism exists regulating the co-evolution between the massive black hole at the center of a galaxy and the formation of its bulge. A possible mechanism of feedback is quasar outflows. Recent theoretical models demonstrate that quasar feedback can serve as a fundamental ingredient in structure formation and galaxy mergers (e.g., Granato et al. 2004; Hopkins et al. 2005; Springel et al. 2005). Quasar outflows could possibly provide an important source of feedback during the growth of the supermassive black-holes (SMBHs) in galactic bulges (e.g., Fabian 1999). Another possible mechanism of feedback may be linked to powerful jets apparently driven by magnetohydrodynamic forces. As observations indicate, these powerful jets are predominantly present in radio-loud (RL) AGNs,<sup>2</sup> which show a tendency to be found in massive galaxies and dense environments (e.g., Best et al. 2005). The importance of jets as a feedback mechanism has been demonstrated with recent *Chandra* observations of cavities in clusters of galaxies and giant elliptical galaxies (e.g., McNamara & Nulsen

2007, and references therein). The injection of power into the Intergalactic Medium (IGM) by radio jets is a promising feedback mechanism that may explain the suppression of cooling flows in the centers of clusters of galaxies (e.g., Fabian et al. 2000; McNamara et al. 2000; Schindler et al. 2001; Heinz et al. 2002). It is not clear, however, if radio jets also contribute to the feedback process in field galaxies, especially ones in the redshift range of  $z = 1 - 3$  where the number density of galaxy mergers is thought to peak. Most clusters of galaxies are not formed until  $z \approx 1$  as inferred from observations (e.g., Hilton et al. 2007) and as predicted in theories that consider a low-density ( $\Omega_m \approx 0.3$ ) Universe (e.g., Bahcall & Fan 1998; Younger et al. 2005). In addition, the fraction of radio-loud AGNs (RLF) appears to evolve with redshift (e.g., Peacock et al. 1986; Schneider et al. 1992; Jiang et al. 2007) and luminosity (e.g., La Franca et al. 1994; Jiang et al. 2007). In particular, the RLF tends to increase with luminosity and decrease with redshift. For example, for luminous AGNs ( $M_{2500} = -26$ ; where  $M_{2500}$  is the absolute magnitude at rest-frame 2500 Å) it is expected that the RLF declines from 24.3% to 4.1% as the redshift increases from 0.5 to 3 (Jiang et al. 2007).<sup>3</sup>

Quasar outflows present a promising mechanism of feedback in high-redshift quasars and possibly in both radio-quiet and radio-loud AGNs. Powerful winds are observed in Broad Absorption Line (BAL) quasars, which show deep and broad absorption features from highly ionized ultraviolet (UV) transitions. BAL quasars are also commonly detected to be X-ray weak as a result of

<sup>1</sup> Department of Astronomy & Astrophysics, Pennsylvania State University, University Park, PA 16802, saez@astro.psu.edu, chartas@astro.psu.edu, niel@astro.psu.edu

<sup>2</sup> Radio-quiet (RQ) AGN in general do not contain large (i.e. kpc) scale collimated jets, although pc-scale jets have been found in some RQ AGNs (e.g., Blundell et al. 1996). Also a fraction ( $\sim 40\%$ ) of radio-quiet AGN could have kpc radio-structures possibly indicating the presence of an “aborted jet” (Gallimore et al. 2006).

<sup>3</sup> As in Jiang et al. (2007) RLF can be written in the form of  $\log[RLF/(1 - RLF)] = b_0 + b_z \log(1 + z) + b_M(M_{2500} + 26)$ , where  $M_{2500}$  is the absolute magnitude at rest-frame 2500 Å,  $b_0 \sim -0.13$ ,  $b_z \sim 2.05$ , and  $b_M \sim 0.18$ .

high intrinsic absorption column densities ( $N_{\text{H}}$ ) typically in the range of  $(1\text{--}50)\times 10^{22} \text{ cm}^{-2}$  (e.g., Gallagher et al. 2002, 2006). We note, however, that a recent survey of BAL quasars obtained from the cross correlation of SDSS and 2XMM catalogs by Giustini et al. (2008) finds no or lower than typical intrinsic X-ray neutral absorption from that found in optically selected BAL quasar samples. In the orientation-based BAL model (e.g., Weymann et al. 1991) quasar winds exist in most quasars; however, because of the relatively small opening angles of these outflows only a fraction of radio-quiet quasars have detectable BAL features in their UV and/or optical spectra. Models based on numerical simulations and observations suggest that the winds of BAL quasars are nearly equatorial (e.g., Murray et al. 1995; Elvis 2000; Proga et al. 2000); however, there are a few observed cases of BAL quasars with outflowing absorbers in the polar direction (e.g., Zhou et al. 2006). Recent studies indicate that BAL quasars comprise  $\sim 15\text{--}40\%$  of the quasar population (e.g., Chartas 2000; Hewett & Foltz 2003; Gibson et al. 2008; Dai et al. 2008).

Our current understanding of AGN physics suggests that the most likely mechanisms to explain the origin of outflows in AGN are thermal driving, radiation driving (line and continuum), and magnetic driving. Thermal driving will produce slow winds (with speeds similar to the sound speed) at large radii ( $\sim 10^4 R_S$ ; where  $R_S = 2GM/c^2$  is the Schwarzschild radius) and with a relatively small mass-loss rate ( $\sim 0.1 M_{\odot} \text{yr}^{-1}$ ) (e.g., Begelman et al. 1983; Krolik et al. 1986). Therefore, in AGNs thermal driving is not expected to produce fast and massive winds and consequently it is likely not a major contributor to feedback.

Given the typical low temperatures of AGN accretion disks ( $T \sim 10^5 \text{ K}$ ) and the large gas densities at the base of winds we expect that initially the absorbing material will have a relatively low ionization parameter. For such conditions radiation-driving can lead to significant acceleration of the absorber. Magnetic driving could also be present in strong AGN winds, through the action of MHD (magnetohydrodynamic) forces (e.g., Everett 2005). In general, we expect MHD and radiation-pressure forces to act jointly with the contribution of radiation pressure becoming increasingly important in sources with higher  $L/L_{\text{Edd}}$  (e.g., Everett 2005, 2007). Dust in the outflow could also boost the radiation pressure depending on the spectral energy distribution (SED) and column density of the material surrounding the AGN (Laor & Brandt 2002; Fabian et al. 2008). At the moment, evidence for the presence of near-relativistic outflows in AGN is accumulating (e.g., Chartas et al. 2002; Reeves et al. 2003; Pounds et al. 2003; Dadina & Cappi 2004; Chartas et al. 2007a; Zheng & Wang 2008)<sup>4</sup>; however, there is no satisfactory model that can produce outflows with the near-relativistic velocities observed (e.g., Murray et al. 1995; Proga et al. 2000; Everett 2005). We note that recent studies (e.g., Chelouche & Netzer 2003; Everett 2005) indicate that

<sup>4</sup> A recent paper by Vaughan & Uttley (2008) suggests that some of the claimed near-relativistic outflows, especially in cases with narrow absorption lines, are detected at moderate significance levels and may be spurious. We note, however, that the statistical significance of the blushifted broad X-ray absorption features detected in APM 08279+5255 and PG 1115+080 is not disputed.

with the appropriate shielding, initial density of the wind, AGN SED and  $L/L_{\text{Edd}}$ , the efficiency of the outflows can be significantly increased and the outflow velocities may approach near-relativistic values.

Due to their high intrinsic absorption, many BAL quasars appear as faint X-ray sources (e.g., Green & Mathur 1996; Gallagher et al. 1999). Partly because of this faintness, it is difficult to detect BALs in X-ray spectra, and as a consequence, there are only a few cases where X-ray BALs have been detected in gravitationally lensed BAL quasars where the magnification effect results in increased signal-to-noise ratio spectra. Observations in X-rays of the BAL quasar APM 08279+5255, the mini-BAL quasar PG 1115+080, and perhaps the low-ionization BAL quasar H 1413–117 have suggested the presence of near-relativistic outflows of X-ray absorbing material in these objects (Chartas et al. 2002, 2003, 2007a,b). The reported variability of the high-energy absorption features is over rest-frame time-scales of 1.8 weeks in APM 08279+5255 (significant detection of variability) and 6 days in PG 1115+080 (marginal detection of variability). The analysis of these high-redshift quasars implied that outflows should have a significant impact in shaping the evolution of their host galaxies and in regulating the growth of the central black hole. These observations are particularly important because they allow us to probe quasar winds at times close to the peak of the comoving number density of luminous quasars.

In this paper we describe the analysis of three recent *Suzaku* observations of the lensed BAL quasar APM 08279+5255. A  $\sim 100$  ks observation of APM 08279+5255 was performed starting on 2006 October 12 (OBS1), a  $\sim 100$  ks observation was performed starting on 2006 November 01 (OBS2), and a  $\sim 120$  ks observation was performed starting on 2007 March 24 (OBS3).

Unless stated otherwise, throughout this paper we use CGS units, the errors listed are at the  $1-\sigma$  level, and we adopt a flat  $\Lambda$ -dominated universe with  $H_0 = 70 \text{ km s}^{-1} \text{ Mpc}^{-1}$ ,  $\Omega_{\Lambda} = 0.7$ , and  $\Omega_M = 0.3$ .

## 2. DATA ANALYSIS

For the reduction and analysis of our observations we used the *Suzaku* software version 7, which is included in HEASOFT version 6.4. To analyze data from the X-ray Imaging Spectrometer (XIS) and the Hard X-ray Detector (HXD) we used calibration files that are part of the *Suzaku* CALDB database released on 2008 April 01.<sup>5</sup>

### 2.1. XIS data analysis

Our data reduction followed the procedures recommended by the *Suzaku* team for Spaced-Row Charge Injection (SCI) data. The data reduction was performed on the event files of each XIS instrument (XIS 0, 1, 2, and 3), and began with recalculating the PI<sup>6</sup> values of the unfiltered event files using the XISPI routine. Once the event

<sup>5</sup> CALDB version 20080401.

<sup>6</sup> Each event has a measured “Pulse Height Amplitude” (PHA). A calculated “PHA Invariant” (PI) value is obtained using the PHA in combination with the instrumental calibration and gain drift. For the XIS, the PI column name is “PI”, which takes values from 0 to 4095. The PI vs. energy relationship is the following:  $E[\text{eV}] = 3.95 \times \text{PI}[\text{channel}]$ .

TABLE 1  
LOG OF OBSERVATIONS OF APM 08279+5255.

Date	OBS ID <sup>a</sup>	Telescope	Instrument	Exposure	Net exp	Net counts <sup>b</sup>	$f_{2-10}^c$
2002-02-24	Cha02 <sup>d</sup>	<i>Chandra</i>	ACIS BI	88.8 ks	...	5723±76	4.3
2002-04-28	Has02 <sup>d</sup>	<i>XMM-Newton</i>	EPIC pn	100.2 ks	...	12928±136	4.0
2006-10-12	701057010	<i>Suzaku</i>	XIS FI	102.3 ks	71.3 ks	7760±88	4.2±0.4
2006-10-12	701057010	<i>Suzaku</i>	XIS BI	102.3 ks	71.3 ks	3046±55	3.5±0.5
2006-11-01	701057020	<i>Suzaku</i>	XIS FI	102.3 ks	67.9 ks	7121±84	3.8±0.3
2006-11-01	701057020	<i>Suzaku</i>	XIS BI	102.3 ks	67.9 ks	2855±78	3.5±0.4
2007-03-24	701057030	<i>Suzaku</i>	XIS FI	117.1 ks	86.4 ks	6059±104	4.0±0.3
2007-03-24	701057030	<i>Suzaku</i>	XIS BI	117.1 ks	86.4 ks	3833±88	3.9±0.3

<sup>a</sup> Throughout this paper we identify the *Suzaku* observations 701057010 as OBS1, 701057020 as OBS2, and 701057030 as OBS3. <sup>b</sup> These counts are obtained in the 0.6–9 keV observed-frame band and in the 0.4–7 keV observed-frame band for the FI and BI chips, respectively. In each *Suzaku* observation, ≈25% of the FI counts and ≈28% of the BI counts are background.<sup>c</sup> The fluxes (in units of  $10^{-13}$  ergs cm $^{-2}$  s $^{-1}$ ) in the 2–10 keV observed-frame band are obtained using the best-fit absorbed power-law model (model 2; §3) in our *Suzaku* observations. The fluxes measured in the BI chips are on average less than those in the FI chips. This is due to a higher half-power-diameter (HPD) of the XIS1 instrument, compared to the HPDs of the XIS0, XIS2, and XIS3 instruments.<sup>d</sup> In this Table we identify as Cha02 the 88.8 ks observation of APM 08279+5255 performed with *Chandra* in 2002 and analyzed in detail in Chartas et al. (2002). We also identify as Has02 the 100.2 ks observation of APM 08279+5255 performed with *XMM-Newton* in 2002 and analyzed in detail in Hasinger et al. (2002).

files were reprocessed, we used the XSELECT software to apply the standard screening criteria (see the *Suzaku* ABC guide<sup>7</sup>) and obtain “cleaned” event files. The data-screening criteria include selecting events corresponding to ASCA grades 0, 2, 3, 4, and 6, Earth elevation angles greater than 5° (ELV>5), Earth day-time elevation angles greater than 20° (DYE\_ELV>20), exclusion of passages through or close to the South Atlantic Anomaly (SAA), and cut-off rigidity criteria of >6  $\frac{\text{GeV}}{\text{c}}$  (COR>6). As a final step in screening the data we removed hot-flickering pixels through the use of the SISCLEAN routine in XSELECT. The total exposure time of each XIS chip decreased by ≈20% after the above screening criteria were applied. Using the clean event files we extracted events in a circular region centered on the source with a radius of 150 pixels (2.5'). Background events were extracted in an annulus centered on the source with an inner radius of ∼230 pixels (3.8') and an outer radius of ∼430 pixels (7.1'). Our selected background region excludes APM 08279+5255 and the calibration sources located near the corners of the CCDs. The response matrix files (RMFs) and ancillary response files (ARFs) were generated using the XISRMFGEN and XISSIMARFGEN routines which include the correction for the hydrocarbon contamination<sup>8</sup> on the optical blocking filter.

For the front-illuminated (FI) XIS chips (XIS 0, 2, 3) we considered events with energies lying in the range 0.6–10 keV, while for the back-illuminated (BI) XIS 1 chip we considered events with energies lying in the range 0.4–8 keV. Due to calibration uncertainties near the CCD Si K absorption edge at 1.84 keV, events with energies lying in the range 1.7–1.95 keV were ignored in the analysis of all four XIS chips. In order to assess systematic uncertainties in the response files, we fitted the Ni K $\alpha$  (7.470 keV) calibration line of each instrument. We found similar positive shifts in the inferred energies of the calibration

lines of each XIS chip ranging from 10 to 20 eV. These shifts in energy were not large enough to cause any significant impact on our analysis, and therefore we did not attempt to correct them. The net source count rate for each XIS chip and each observation was ≈0.04 counts s $^{-1}$ , with a background of ≈30 % of the source rate. The spectra obtained on the FI chips were combined using the routine ADDSPEC (in HEASOFT FTOOLS) in order to increase their signal-to-noise ratio. In Table 1 we have included information relevant to the XIS data analysis. Specifically, this table lists the observation ID, exposure time, net exposure time (after the screening process), net counts (for the FI and BI chips) and flux in the 2–10 keV observed-frame (for the FI and BI chips) using the best-fitted absorbed power-law model (model 2; §3). We also have included in Table 1 information from two previous deep X-ray observations of APM 08279+5255. These observations correspond to an 88.8 ks *Chandra* exposure (see Chartas et al. 2002) and to a 100.2 ks *XMM-Newton* exposure (see Hasinger et al. 2002). The counts collected by the XIS FI chips for each of our observations are comparable to those obtained in the *Chandra* observation.

## 2.2. HXD data Analysis

Similarly to the XIS case the clean event files were obtained from the unfiltered event files following the instructions in the *Suzaku* ABC guide. The screening criteria are similar to those applied to the XIS instruments, specifically, we used ELV>5°, DYE\_ELV>20°, exclusion of passages close to the SAA, and COR>6 (units of  $\frac{\text{GeV}}{\text{c}}$ ). The HXD-PIN spectrum was extracted from the cleaned events file described above. We extracted the source spectra from the clean files XSELECT. In order to estimate non X-ray background (NXB) events, we used version 2 of a time-dependent instrumental background event file (referred to as the PIN background event file) which was provided by the *Suzaku* team. The PIN background event file was generated with a count rate that is ten times larger than the real instrumental PIN background. Therefore, we increased the effective exposure time of our observed PIN background spectra

<sup>7</sup> <http://heasarc.gsfc.nasa.gov/docs/suzaku/analysis/abc/>

<sup>8</sup> The XISSIMARFGEN routine incorporates the XISCONTAM-ICALC routine which is used to correct the observation for the XIS optical blocking filter (OBF) contamination. The absorption due to these contaminants depends on the X-ray energy, time, detector ID and location on the detector.

TABLE 2  
LOG OF PIN HXD *Suzaku* OBSERVATIONS OF APM 08279+5255.

Epoch	Net exposure	10–40 keV count rate ( $10^{-2} \text{cts s}^{-1}$ )		
		source	NXB	CXB <sup>a</sup>
OBS1	88 ks	$49.75 \pm 0.24$	$48.17 \pm 0.07$	$2.30 \pm 0.05$
OBS2	89 ks	$50.37 \pm 0.24$	$46.05 \pm 0.07$	$2.39 \pm 0.05$
OBS3	103 ks	$47.07 \pm 0.21$	$44.12 \pm 0.06$	$2.29 \pm 0.05$

<sup>a</sup> The CXB counts have been estimated from a fake spectrum generated using the FAKEIT command of XSPEC with the model given in equation (1).

by a factor of ten. The exposure time was corrected for dead time using the HXDDTCOR task, leaving an effective exposure time of  $\sim 90\%$  of the original exposure time. The effective exposure time of each observation, together with the count rates (10–40 keV) of the source and NXB are presented in Table 2. The NXB does not include the contribution from cosmic X-ray background (CXB). Therefore the CXB counts (see Table 2) have been estimated from a fake spectrum generated using the FAKEIT command of XSPEC with the following model (e.g., Boldt 1987):

$$\frac{CXB(E)}{9.412 \times 10^{-3}} = e^{-\frac{E}{40\text{keV}}} \left( \frac{E}{1\text{keV}} \right)^{-1.29} \text{cm}^{-2}\text{s}^{-1}\text{sr}^{-1}\text{keV}^{-1}. \quad (1)$$

The response file used to fit the PIN spectra was obtained from the *Suzaku* CALDB calibration files. The HXD spectral analysis was performed in the 10–40 keV energy range.

### 3. SPECTRAL ANALYSIS

In this section we fit the *Suzaku* spectra of APM 08279+5255 with a variety of models using the software tool XSPEC version 12. We also fit the spectra with more realistic models based on the photoionization code XSTAR. In all spectral models we assume a Galactic column density of  $4.1 \times 10^{20} \text{ cm}^{-2}$  (Kalberla et al. 2005). Most of this section concentrates on the analysis of the XIS spectra; however, in the last paragraph we present results from the spectral analysis of the PIN spectra of APM 08279+5255.

#### 3.1. XIS spectral fits.

##### 3.1.1. XSPEC spectral fits.

Each observation of APM 08279+5255 provides spectra obtained with the single BI chip (XIS1) and the FI chips (XIS 0, 2, and 3). Since the responses of the FI chips are similar we co-added the FI spectra from each observation. We note that there is no XIS 2 spectrum of APM 08279+5255 for our third epoch (OBS3) due to the failure of the XIS2 chip.<sup>9</sup> To fit the spectra using  $\chi^2$  statistics we grouped each XIS spectrum with a sufficient number of counts. The minimum number of counts per bin was also chosen to maximize the signal-to-noise ratio in each bin without losing the features in the spectra and to keep a similar number of spectral bins in each

<sup>9</sup> On 2006 November 9, about 2/3 of the imaging area of XIS2 became suddenly unusable (<http://heasarc.gsfc.nasa.gov/docs/suzaku/news/xis2.html>).

spectrum ( $\approx 70$ ). The minimum number of counts per bin chosen for the BI chip was 40 for epochs OBS1 and OBS2 and 50 for epoch OBS3. The grouping for the FI chips was 100 counts per bin for epochs OBS1 and OBS2 and 80 counts per bin for epoch OBS3. Note that for epoch OBS3 we have increased the binning of the BI spectra due to the longer exposure and decreased the binning of the FI spectra to compensate for the loss of XIS2.

We fit the spectra of APM 08279+5255 with the following models: 1) power-law (PL; XSPEC model wabs\*pow), 2) absorbed power-law (APL; XSPEC model wabs\*zwabs\*pow), 3) ionized-absorbed power-law (IAPL; XSPEC model wabs\*absori\*pow), 4) partially covered absorbed power-law (PAPL; XSPEC model wabs\*zpcfabs\*pow), 5) absorbed power-law with a notch (APL+No; XSPEC model wabs\*zwabs\*notch\*pow), 6) absorbed power-law with an absorption edge (APL+Ed; XSPEC model wabs\*zwabs\*zedge\*pow), and 7) absorbed power-law with two absorption lines (APL+2AL<sup>10</sup>; XSPEC model wabs \* zwabs \* [pow + zgauss + zgauss]).

The results of the FI and BI fits with the models described are listed in Table 3. The error bars of the fitted parameters are given at the 68% level ( $\Delta\chi^2 = 1$ ). For models 2 to 7 we assume an intrinsic absorber with a redshift of 3.91 (Downes et al. 1999). The fits using a power-law model (model 1) are not acceptable in a statistical sense. We next fit the spectra of APM 08279+5255 with the absorbed power-law model (model 2; Table 3) assuming an intrinsic absorber. The *F*-test indicates that fits with model 2 result in a significant improvement at the  $\gtrsim 99\%$  and  $\gtrsim 99.9\%$  confidence levels in the FI and BI spectra, respectively, compared to fits using model 1. Fits with model 2 indicate significant intrinsic absorption in APM 08279+5255 with a column density of  $\log N_{\text{H}} \approx 23$ . We also fit the spectra of APM 08279+5255 with more complex models that included an ionized and partially covered absorber (models 3 and 4), however, these fits did not result in a significant improvement (*F*-test significance  $< 95\%$ ) compared to the simpler model 2.

Fits to the spectra of APM 08279+5255 with models (models 5–7) that account for the absorption found between 7–12 keV in the rest-frame result in significant improvements (the *F*-test indicates improvements at  $\gtrsim 99.9\%$  and  $\gtrsim 99\%$  confidence in the FI and BI spectra, respectively) compared to fits with models that do not include this high-energy absorption. We note that the absorption feature at 7–12 keV in the rest-frame corresponds to a significant detection following the criteria described in §3 of Vaughan & Uttley (2008). Specifically, we find the ratio of the total equivalent width<sup>11</sup> of the absorption features to their uncertainty to be  $EW/\sigma_{EW} \gtrsim 3$  in every observation (see models 5–7 in Table 3).

<sup>10</sup> We note that if we replace the APL+2AL model by the XSPEC absorption-line multiplicative model wabs\*zwabs\*gabs(pow), we obtain similar results for the fitted energies and equivalent widths of the absorption features found at energies 7–12 keV in the rest-frame. All the results described in this paper using the APL+2AL can be reproduced using this multiplicative model.

<sup>11</sup> The equivalent width (EW) is defined as  $EW = \int \frac{F_c - F_E}{F_c} dE$ , where  $F_c$  is the continuum flux and  $F_E$  is the flux in the absorber.

TABLE 3  
RESULTS FROM SPECTRAL FITS TO THE THREE *Suzaku* OBSERVATIONS OF APM 08279+5255.

Model <sup>a</sup>	Parameter	FI SPECTRUM <sup>b</sup>			BI SPECTRUM <sup>b</sup>		
		Values OBS 1	Values OBS 2	Values OBS 3	Values OBS 1	Values OBS 2	Values OBS 3
1.....	$\Gamma$	1.70 $^{+0.02}_{-0.02}$	1.75 $^{+0.03}_{-0.03}$	1.77 $^{+0.03}_{-0.03}$	1.67 $^{+0.04}_{-0.04}$	1.58 $^{+0.05}_{-0.05}$	1.61 $^{+0.04}_{-0.04}$
	$\chi^2/\nu$	118.3/73	125.8/66	99.1/71	114.0/71	140.8/66	100.6/71
	$P(\chi^2/\nu)$	$6 \times 10^{-4}$	$1 \times 10^{-5}$	0.02	$9 \times 10^{-4}$	$2 \times 10^{-7}$	0.01
2.....	$\Gamma$	1.89 $^{+0.04}_{-0.03}$	1.98 $^{+0.04}_{-0.04}$	1.88 $^{+0.05}_{-0.05}$	1.96 $^{+0.07}_{-0.07}$	1.93 $^{+0.07}_{-0.07}$	1.92 $^{+0.06}_{-0.06}$
	$\log N_{\text{H}}$	22.83 $^{+0.09}_{-0.10}$	22.92 $^{+0.09}_{-0.10}$	22.66 $^{+0.15}_{-0.20}$	22.74 $^{+0.09}_{-0.09}$	22.78 $^{+0.09}_{-0.10}$	22.75 $^{+0.09}_{-0.09}$
	$\chi^2/\nu$	90.5/72	87.9/65	91.0/70	86.7/70	101.3/65	59.0/70
	$P(\chi^2/\nu)$	0.07	0.03	0.05	0.59	$3 \times 10^{-3}$	0.82
3.....	$\Gamma$	1.90 $^{+0.04}_{-0.05}$	1.99 $^{+0.05}_{-0.05}$	1.90 $^{+0.05}_{-0.05}$	1.97 $^{+0.07}_{-0.07}$	1.94 $^{+0.08}_{-0.08}$	1.94 $^{+0.07}_{-0.07}$
	$\log N_{\text{H}}$	22.92 $^{+0.08}_{-0.07}$	22.99 $^{+0.07}_{-0.09}$	22.80 $^{+0.13}_{-0.15}$	22.79 $^{+0.11}_{-0.11}$	22.87 $^{+0.16}_{-0.12}$	22.93 $^{+0.08}_{-0.15}$
	$\log \xi$	<0.18	<0.11	<0.75	<0.22	<0.68	<0.98
	$\chi^2/\nu$	86.0/71	83.2/64	87.6/69	84.4/70	99.7/64	56.6/69
4.....	$P(\chi^2/\nu)$	0.11	0.05	0.06	0.12	$3 \times 10^{-3}$	0.86
	$\Gamma$	1.90 $^{+0.07}_{-0.07}$	2.00 $^{+0.07}_{-0.08}$	1.91 $^{+0.09}_{-0.09}$	1.96 $^{+0.08}_{-0.09}$	1.92 $^{+0.09}_{-0.08}$	1.91 $^{+0.06}_{-0.06}$
	$\log N_{\text{H}}$	22.85 $^{+0.18}_{-0.10}$	23.01 $^{+0.20}_{-0.15}$	22.71 $^{+0.22}_{-0.16}$	22.75 $^{+0.11}_{-0.10}$	22.79 $^{+0.12}_{-0.10}$	22.75 $^{+0.12}_{-0.07}$
	CF	0.95 $^{+0.05}_{-0.32}$	0.89 $^{+0.11}_{-0.22}$	0.92 $^{+0.08}_{-0.26}$	0.95 $^{+0.05}_{-0.11}$	0.94 $^{+0.06}_{-0.08}$	0.93 $^{+0.07}_{-0.08}$
	$\chi^2/\nu$	86.9/71	85.6/64	88.9/69	85.4/70	100.9/64	57.9/69
5.....	$P(\chi^2/\nu)$	0.10	0.04	0.05	0.10	$2 \times 10^{-3}$	0.82
	$\Gamma$	1.95 $^{+0.04}_{-0.04}$	1.98 $^{+0.04}_{-0.04}$	1.91 $^{+0.05}_{-0.03}$	1.95 $^{+0.06}_{-0.06}$	1.91 $^{+0.07}_{-0.07}$	1.92 $^{+0.06}_{-0.06}$
	$\log N_{\text{H}}$	22.95 $^{+0.06}_{-0.07}$	22.98 $^{+0.08}_{-0.08}$	22.82 $^{+0.10}_{-0.13}$	22.80 $^{+0.08}_{-0.07}$	22.83 $^{+0.08}_{-0.09}$	22.80 $^{+0.07}_{-0.06}$
	$E_{\text{notch}} [\text{keV}]$	9.59 $^{+0.17}_{-0.15}$	9.75 $^{+0.25}_{-0.24}$	9.40 $^{+0.29}_{-0.20}$	9.81 $^{+0.26}_{-0.25}$	10.41 $^{+0.56}_{-0.61}$	9.96 $^{+0.39}_{-0.42}$
	$W_{\text{notch}} [\text{keV}]$	3.98 $^{+0.35}_{-0.32}$	3.86 $^{+0.47}_{-0.53}$	4.03 $^{+0.44}_{-0.39}$	4.71 $^{+0.88}_{-0.93}$	5.01 $^{+0.91}_{-0.96}$	4.52 $^{+0.93}_{-0.88}$
	$f_{\text{notch}} [\text{keV}]$	0.20 $^{+0.04}_{-0.05}$	0.18 $^{+0.05}_{-0.05}$	0.17 $^{+0.05}_{-0.04}$	0.26 $^{+0.05}_{-0.05}$	0.21 $^{+0.05}_{-0.06}$	0.18 $^{+0.05}_{-0.05}$
6.....	$EW_{\text{notch}} [\text{keV}]^c$	0.80 $\pm$ 0.21	0.70 $\pm$ 0.22	0.69 $\pm$ 0.21	1.22 $\pm$ 0.33	1.05 $\pm$ 0.36	0.81 $\pm$ 0.28
	$\chi^2/\nu$	62.3/69	70.6/62	74.2/67	58.1/67	90.8/62	48.1/67
	$P(\chi^2/\nu)$	0.70	0.21	0.26	0.77	0.01	0.96
	$\Gamma$	1.93 $^{+0.04}_{-0.04}$	2.00 $^{+0.03}_{-0.04}$	1.93 $^{+0.05}_{-0.05}$	1.94 $^{+0.07}_{-0.07}$	1.88 $^{+0.07}_{-0.07}$	1.90 $^{+0.06}_{-0.06}$
7.....	$\log N_{\text{H}}$	22.94 $^{+0.07}_{-0.08}$	23.00 $^{+0.06}_{-0.08}$	22.82 $^{+0.11}_{-0.13}$	22.80 $^{+0.08}_{-0.08}$	22.81 $^{+0.08}_{-0.09}$	22.79 $^{+0.07}_{-0.08}$
	$E_{\text{zedge}} [\text{keV}]$	7.71 $^{+0.15}_{-0.14}$	8.06 $^{+0.17}_{-0.29}$	7.48 $^{+0.12}_{-0.13}$	7.47 $^{+0.13}_{-0.13}$	8.32 $^{+0.52}_{-0.33}$	7.74 $^{+0.20}_{-0.23}$
	$\tau_{\text{zedge}}$	0.32 $^{+0.07}_{-0.07}$	0.30 $^{+0.08}_{-0.08}$	0.31 $^{+0.08}_{-0.08}$	0.56 $^{+0.18}_{-0.19}$	0.46 $^{+0.17}_{-0.18}$	0.41 $^{+0.13}_{-0.12}$
	$EW_{\text{zedge}}^c$	1.19 $\pm$ 0.28	1.12 $\pm$ 0.28	1.09 $\pm$ 0.26	1.86 $\pm$ 0.59	1.54 $\pm$ 0.64	1.42 $\pm$ 0.42
	$\chi^2/\nu$	67.1/70	71.1/63	74.3/68	64.3/68	91.0/63	46.1/68
	$P(\chi^2/\nu)$	0.58	0.23	0.28	0.60	0.01	0.98

<sup>a</sup> Model 1 is a power-law with Galactic absorption (PL; XSPEC model wabs\*pow); Model 2 is a power-law with Galactic absorption and intrinsic absorption (APL; XSPEC model wabs\*zwabs\*pow); Model 3 is a power-law with Galactic absorption and ionized-absorption (IAPL; XSPEC model wabs\*absori\*pow); Model 4 is power-law with Galactic absorption and partially covered absorption (PAPL; XSPEC model wabs\*zpcfabs\*pow); Model 5 is a power-law with Galactic absorption, intrinsic absorption, and a notch absorber (APL+No; XSPEC model wabs\*zwabs\*notch\*pow); Model 6 is a power-law with Galactic absorption, intrinsic absorption, and an absorption edge (APL+Ed; XSPEC model wabs\*zwabs\*zedge\*pow); Model 7 is a power-law with Galactic absorption, intrinsic absorption, and two absorption lines (APL+2AL; XSPEC model wabs \* zwabs \* [pow + zgauss + zgauss]). <sup>b</sup> The spectra fitted are the added (ftools ADDSPEC) spectra of the FI chips (XIS0, XIS2 and XIS3). For OBS 2 the XIS2 CCD was not operational, and only the XIS0 and XIS3 spectra were added for this observation. The BI spectra are taken with the XIS1 chip. <sup>c</sup> EW stands for equivalent width, which is defined as  $EW = \int \frac{F_c - F_E}{F_c} dE$ , where  $F_c$  is the continuum flux and  $F_E$  is the flux in the absorber.

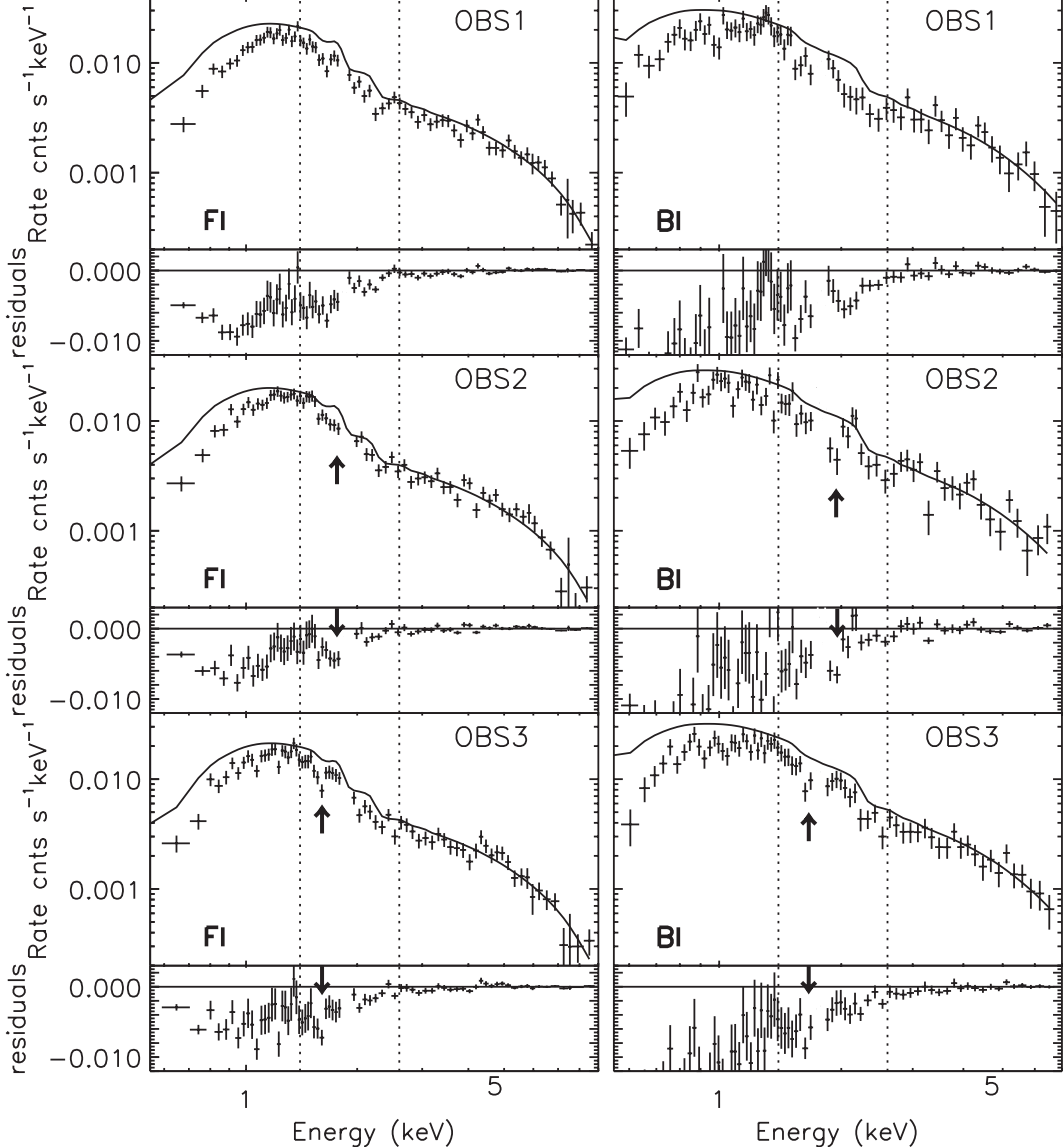


FIG. 1.— *Suzaku* FI (left panel) and BI (right panel) spectra of the combined images of APM 08279+5255 for the three observations (OBS 1, 2, and 3), fit with Galactic absorption and a power-law model to events with observed-frame energies above 3.6 keV and then extrapolated to lower energies. In the lower panel of each observation, we show the residuals of the fit with  $1-\sigma$  error bars. High-energy absorption features are detected within the 7–12 keV range (dotted lines). We have marked with an arrow the best-fitted energies of the first absorption feature of model 7 for epochs OBS2 and OBS3. For the FI spectra the grouping in OBS1 and OBS2 is 100 counts per bin, and in OBS 3 it is 80 counts per bin. For the BI spectra the grouping in OBS1 and OBS2 is 40 counts per bin, and in OBS3 it is 50 counts per bin.

To illustrate the presence of the high-energy absorption features, we fit the spectra from observed-frame energies of 3.6–10 keV with a power-law model and extrapolated this model to the energy ranges not fit (see Figure 1). The lower panels in Figure 1 show the residuals (difference between the measured counts and model) between the best-fit power-law model and the FI and BI data, respectively. The best-fit values of the photon indices in all observations with this model were consistent with  $\Gamma = 2$  at the  $1-\sigma$  level. For the purpose of comparing the absorption residuals between epochs the photon indices for all observations were set to  $\Gamma = 2.0$ . From these fits we notice that the residuals show an absorption feature centered near a rest-frame energy of  $\sim 8$  keV and a possible second absorption feature near a rest-frame energy of  $\sim 10$  keV. We fit the high-energy absorption features with the models listed in Table 3. From these fits we found that adding to the APL model an absorption edge (APL+Ed) or two absorption lines (APL+2AL) improves the fits at the  $\gtrsim 99\%$  confidence level in the two sets of spectra (FI and BI) and in each observation. The  $F$ -test indicates that we cannot distinguish between the (APL+Ed) and (APL+2AL) models for fits performed to the spectra of APM 08279+5255 in epochs OBS2 and OBS3, since both models fit equally well the 7–12 keV rest-frame absorption during these epochs.<sup>12</sup> However, fits to the FI and BI spectra of epoch OBS1 using the APL+2AL model provide a significant improvement at the 95% and 98% confidence levels, respectively, compared to fits that use the APL+Ed model. It is important to note that the APL+2AL model was clearly favored over the APL+Ed model in a previous 88.8 ks *Chandra* observation (Chartas et al. 2002). Fits to the spectra in epoch OBS1 with a model that includes an absorption notch (see Table 3) also provide a significant improvement compared to ones using the APL+Ed model. These  $F$ -test improvements are at the  $\sim 98\%$  and  $\sim 99\%$  levels of significance in the FI and BI spectra, respectively. We note, however, that when we compare the quality of the spectral fits that use the APL+Ed model with fits that use either the APL+2AL or APL+notch models, the  $F$ -test may not be a reliable tool. The reason for the non-reliability of the  $F$ -test is that we are not comparing nested models (see Protassov et al. 2002 for details). In order to check the reliability of the  $F$ -test for these cases, we performed Monte Carlo simulations of 10,000 fake spectra (using the FAKEIT command of XSPEC) assuming an APL+Ed model. In these simulations, the energy and optical depth of the absorption edge are assumed to be normally distributed around their fitted values for epoch OBS1 (see model 6 of Table 3), with a standard deviation given by the error bars of the fits. All other parameters of the APL+Ed model were set to their best-fitted values (epoch OBS1 and model 6 of Table 3). The results of our Monte Carlo analysis are presented in Table 4. In each simulation we have fitted the data with the null model (APL+Ed) and the alternative model (either APL+2AL or APL+notch). We then

<sup>12</sup> We only find marginal improvements in fits to the spectra of APM 08279+5255 taken in epochs OBS2 and OBS3 using model 7 (APL+2AL) compared to fits using model 6 (APL+Ed). Specifically, in epoch OBS2 these improvements are at the 61% and 91% significance levels in the FI and BI, and in epoch OBS3 they are at the 68% and 50% significance levels.

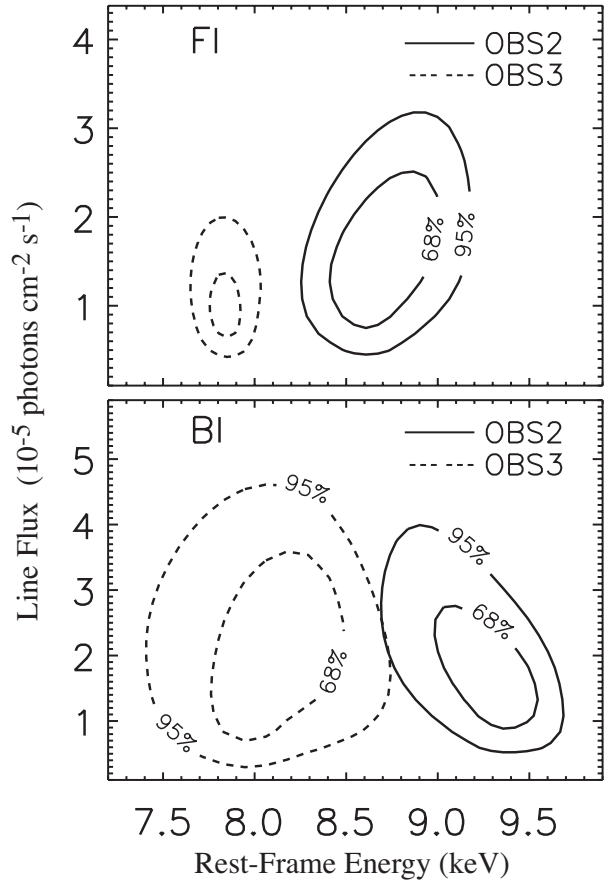


FIG. 2.— 68% and 95% confidence contours of absorption-line fluxes versus absorption-line energies of the first modeled absorption line (model 7, Table 3). The upper and lower panel contours correspond to fits performed to the FI and BI spectra, respectively. Solid and dotted lines are contours for epochs OBS2 and OBS3, respectively.

calculated the value of the  $F$ -statistic between the null model and the alternative model. In Table 4 we show that the  $p$ -value, which represents the fraction of simulated cases with values of the  $F$ -statistic higher than the actual value obtained from our real data, is similar to the null probability of the  $F$ -test. We therefore conclude that our  $F$ -test values are reliable and are approximately representative of the improvement of the alternative model (either APL+2AL or APL+notch) with respect to the null model (APL+Ed).

The results of the spectral fits shown in Table 3 indicate a change (greater than  $1-\sigma$ ) of the energies of the best-fit values of the first absorption line (abs1; model 7), and in the absorption-edge energy ( $E_{\text{Edge}}$ ; model 6) between epochs OBS2 and OBS3 in both the FI and BI spectra. This change is also suggested by the residuals in Figure 1, where we have marked with an arrow the best-fitted energies of the first absorption feature of model 7 for epochs OBS2 and OBS3. The shift in the energy of the first absorption line is indicative of possible variability of the outflow. This change can be seen more clearly in Figure 2 where we show the  $\chi^2$  confidence contours of the best-fit energies of the first absorption line (APL + 2AL model) versus its line-flux normalization in epoch OBS2 (solid line) and in epoch OBS3 (dotted line).<sup>13</sup>

<sup>13</sup> We note that for the FI spectra of APM 08279+5255 during

TABLE 4  
ESTIMATES OF THE IMPROVEMENT OF FITS TO THE SPECTRA OF  
APM 08279+5255 USING ALTERNATIVE MODELS TO THE APL+EDGE MODEL.

Alternative model	Spectrum <sup>a</sup>	<i>F</i> -statistic/null probability <sup>b</sup>	<i>p</i> <sup>c</sup>
APL+2AL	FI	2.59 / $4.4 \times 10^{-2}$	$5.2 \times 10^{-2}$
APL+2AL	BI	3.05 / $2.3 \times 10^{-2}$	$3.1 \times 10^{-2}$
APL+notch	FI	5.32 / $2.4 \times 10^{-2}$	$6.8 \times 10^{-2}$
APL+notch	BI	7.15 / $0.9 \times 10^{-2}$	$3.9 \times 10^{-2}$

<sup>a</sup> The XIS FI and BI spectra of APM 08279+5255 considered in this comparison are taken from epoch OBS1. <sup>b</sup> The value on the left of the slash is the *F*-statistic and is given by  $F = \frac{x_{\nu_1}^2 - x_{\nu_1}^2}{\Delta\nu} / \frac{x_{\nu_2}^2}{\nu_2}$ . The value on the right of the slash represents the probability of exceeding the *F*-statistic based on the *F*-test. <sup>c</sup> The *p*-value represents the probability of exceeding the *F*-statistic based on our Monte Carlo simulations. The value of the *F*-statistic is obtained by comparing the null model (APL+Edge) with the alternative model listed in the first column for fits performed to the spectra of APM 08279+5255 obtained in epoch OBS1.

In the upper and lower panels of Figure 2, we show the  $\chi^2$  confidence contours of the FI and the BI spectra, respectively. The confidence contours touch at the  $\sim 99\%$  level of significance for the FI spectra and at the  $\sim 95\%$  level of significance for the BI spectra. The probabilities that the flux-energy parameters of the first absorption line (model 7; Table 3) are the same between OBS2 and OBS3 (null probabilities) are  $\lesssim 1 \times 10^{-4}$  and  $\lesssim 2.5 \times 10^{-3}$  in the FI spectra and BI spectra, respectively.<sup>14</sup> To take into account possible sampling effects caused by the number of trials used in our variability analysis we multiply the null probabilities by six. This factor corresponds to the number of absorption lines (two) times the number of observations (three). We conclude that the variability of the first absorption line is significant at the  $\gtrsim 99.9\%$  and  $\gtrsim 98\%$  levels in the FI and BI spectra, respectively.

We note that the slight differences ( $< 68\%$  significance) between the FI and BI confidence contours may possibly be associated with differences in the responses, variations in the signal-to-noise ratios of the two detectors, and statistical noise.

### 3.1.2. XSTAR spectral fits.

The spectral analysis presented in §3.1.1 indicates that the intrinsic X-ray absorbing medium of APM 08279+5255 is complex and contains absorbers with different properties (see models 5–7 in Table 3). We identified a low-ionization absorber with a column density of  $\log N_{\text{H}} \sim 23$  and an ionization parameter of  $\log \xi \lesssim 0$ <sup>15</sup> (see models 2–4 in Table 3). This low-ionization absorber is required to model the absorption detected below  $\sim 2$  keV (observed-frame). An additional complex absorber is required to fit the broad absorption features with rest-frame energies between

epoch OBS2, the first absorption feature (abs1) falls near the Si K edge where events with energies lying in the range 1.7–1.95 keV were ignored in the analysis. Although the loss of these data points adds a larger statistical error to the best-fitted parameters of abs1, it does not significantly affect the analysis. Specifically, this error in the best-fitted energies is less than the value of  $\sigma_{\text{abs1}}$  and more likely close to  $\frac{\sigma_{\text{abs1}}}{2} \sim 0.2$  keV (see Table 3).

<sup>14</sup> The square of the probabilities of being outside the confidence contours that barely touch (see Figure 2) is an upper limit to the null probabilities.

<sup>15</sup> The spectral fits did not show an improvement using a warm-absorber model; however the  $\lesssim 4$  keV absorption was not well constrained since the *Suzaku* spectra start at rest-frame energies of  $E \sim 2$  keV.

7–12 keV. Given the range of energies and variability of the broad absorption features, we interpret this absorption as a blend of highly ionized ( $2.75 \lesssim \log \xi \lesssim 4$ ) iron absorption lines blueshifted by an outflow. This explanation is consistent with recent models that attempt to simulate X-ray BALs in quasars (e.g., Schurch & Done 2007). To test this interpretation we next employ more complex, but more realistic, models to fit the APM 08279+5255 spectra.

As a first attempt we fit the low and high-energy absorption of APM 08279+5255 in epoch OBS1 with a model that includes a power-law (with Galactic absorption) and one warm absorber (model XSTAR1, Table 5). The warm-absorber model is calculated using the XSTAR code (see, e.g., Kallman & Bautista 2001; Kallman et al. 1996). XSTAR calculates the physical conditions and absorption-emission spectra of photoionized gases with variable abundances. In the current analysis we use a recent implementation of the XSTAR code called WARMABS that can be used as a model within XSPEC. For the WARMABS model we assume turbulent velocities  $v_{\text{turb}} = 1,000$  km s $^{-1}$  (default velocity of the model).<sup>16</sup> For the fits we assumed solar abundances, a redshift of 3.91 for the warm absorber, and we left the column density and ionization parameter of the warm absorber free to vary in the fit. We note that spectral fits using model XSTAR1 attempt to fit both the low and high-energy absorption of APM 08279+5255 with a single warm absorber.

To constrain the iron abundance ( $a_{\text{Fe}}$ ), we allowed this parameter to vary in the spectral fits in the model XSTAR2. The only difference between models XSTAR1 and XSTAR2 is that  $a_{\text{Fe}}$  is fixed in model XSTAR1 and free to vary in model XSTAR2. We find that allowing  $a_{\text{Fe}}$  to vary in our spectral fits does not lead to a significant improvement in the fits, and the best-fit values of  $a_{\text{Fe}}$  in fits with model XSTAR2 are consistent with no iron over-abundance. Our results do not confirm an apparent iron over-abundance ( $a_{\text{Fe}} > 2$ ) claimed by Hasinger et al. (2002) and Ramírez (2008) based on their analyses of previous observations of APM 08279+5255.

We next assumed the spectral model XSTAR3 consist-

<sup>16</sup> Since a warm absorber with  $\log \xi \sim 1.0$  is expected to have a temperature of  $\lesssim 10^6$  K (e.g., Chelouche & Netzer 2003), we do not expect a thermal broadening higher than 100 km s $^{-1}$ .

TABLE 5  
RESULTS FROM SPECTRAL FITS USING XSTAR TO EPOCHS OBS1, OBS2 AND OBS3 OF APM 08279+5255.

XSPEC Model	Parameter	OBS1		OBS2		OBS3	
		Values FI	Values BI	Values FI	Values BI	Values FI	Values BI
XSTAR1.....	$\Gamma$	1.96±0.04	1.99±0.05	2.00±0.05	1.96±0.07	1.97±0.05	1.95±0.06
	$\log N_{\text{H}}$	23.35±0.08	23.19±0.10	23.30±0.09	23.28±0.12	23.25±0.09	23.26±0.08
	$\log \xi$	1.02±0.52	0.45±0.36	0.99±0.52	1.76±0.62	1.05±0.75	1.51±0.66
	$\chi^2/\nu$	69.1/71	70.7/69	82.0/64	92.7/64	73.8/69	48.2/69
	$P(\chi^2/\nu)^c$	0.54	0.42	0.06	0.01	0.32	0.97
XSTAR2.....	$\Gamma$	1.94±0.05	2.00±0.07	2.01±0.05	1.95±0.07	1.97±0.05	1.95±0.06
	$\log N_{\text{H}}$	23.30±0.09	23.18±0.10	23.40±0.08	23.24±0.12	23.25±0.09	23.26±0.08
	$\log \xi$	1.09±0.51	0.54±0.42	1.28±0.65	1.70±0.78	1.05±0.75	1.51±0.66
	$a_{\text{Fe}}$	1.1±0.3	1.8±0.5	0.6±0.2	1.2±0.5	1.0±0.3	1.0±0.4
	$\chi^2/\nu$	68.7/70	65.2/68	77.1/63	92.5/63	73.8/68	48.2/68
XSTAR3.....	$\Gamma$	1.97±0.05	1.96±0.08	2.02±0.05	1.95±0.07	1.96±0.05	1.92±0.06
	$\log N_{\text{Habs}1}$	23.31±0.09	23.17±0.18	23.40±0.08	23.28±0.10	23.21±0.09	23.14±0.09
	$\log \xi_{\text{abs}1}$	1.17±0.55	0.50±0.36	1.26±0.47	1.28±0.25	0.78±0.46	1.31±0.49
	$a_{\text{Fe}}$	0.8±0.2	1.5±0.7	0.6±0.3	1.2±0.6	1.1±0.3	1.3±0.5
	$z_{\text{abs}1}$	3.91	3.91	3.91	3.91	3.91	3.91
	$\log N_{\text{Habs}2}$	23.07±0.31	23.36±0.26	22.79±0.36	22.87±0.41	22.91±0.35	23.21±0.39
	$\log \xi_{\text{abs}2}$	3.7±0.4	3.6±0.5	3.5±0.3	3.8±0.5	3.5±0.4	3.7±0.5
	$z_{\text{abs}2}$	2.06±0.05	2.18±0.08	1.98±0.07	1.79±0.12	2.19±0.13	2.07±0.10
	$\chi^2/\nu$	58.0/67	54.9/65	73.6/60	89.8/60	70.2/65	43.6/65
XSTAR4.....	$\Gamma$	1.94±0.06	1.95±0.07	2.01±0.05	1.92±0.07	1.93±0.05	1.91±0.07
	$\log N_{\text{Habs}1}$	22.86±0.16	23.01±0.26	22.93±0.31	23.16±0.36	22.82±0.21	23.02±0.28
	$\log \xi_{\text{abs}1}$	3.8±0.3	3.5±0.2	3.6±0.2	3.8±0.5	3.1±0.3	3.3±0.3
	$z_{\text{abs}1}$	3.08±0.10	3.22±0.12	2.78±0.08	2.57±0.12	3.24±0.06	3.12±0.08
	$(\frac{v}{v_{\text{abs}1}})^b$	(0.19±0.02)	(0.16±0.03)	(0.27±0.02)	(0.32±0.03)	(0.15±0.01)	(0.18±0.02)
	$\log N_{\text{Habs}2}$	23.38±0.15	23.43±0.22	22.91±0.35	23.09±0.39	23.10±0.38	23.07±0.41
	$\log \xi_{\text{abs}2}$	3.6±0.5	3.4±0.2	3.4±0.3	3.7±0.6	3.5±0.3	3.6±0.6
	$z_{\text{abs}2}$	2.10±0.06	2.17±0.08	1.97±0.09	1.78±0.13	2.18±0.12	2.05±0.10
	$(\frac{v}{v_{\text{abs}1}})^b$	(0.45±0.02)	(0.43±0.02)	(0.48±0.02)	(0.53±0.03)	(0.42±0.03)	(0.46±0.03)
	$\chi^2/\nu$	56.3/66	55.1/64	65.1/59	80.0/59	67.1/64	43.4/64
	$P(\chi^2/\nu)^c$	0.80	0.78	0.27	0.04	0.37	0.98

<sup>a</sup> XSTAR1≡ XSPEC model warmabs(pow); XSTAR2≡ XSPEC model warmabs(pow) (FeA variable); XSTAR3≡ XSPEC model warmabs\*warmabs(pow); XSTAR4≡ XSPEC model wabs\*zwabs\*warmabs\*warmabs(pow) <sup>b</sup>  $\frac{v}{v_{\text{abs}1}}$  and  $\frac{v}{v_{\text{abs}2}}$  corresponds to the estimated outflow velocities. They are calculated from equation 2 based on the redshift of the absorbers of model XSTAR4. They are not parameters of the spectral fit.<sup>c</sup> Probability that  $\chi^2/\nu$  is greater than the value obtained.

ing of a power-law, one stationary ionized absorber with a turbulent velocity of  $v_{\text{turb}} = 1,000 \text{ km s}^{-1}$  and a second outflowing ionized absorber with a turbulent velocity of  $v_{\text{turb}} = 10,000 \text{ km s}^{-1}$  (the maximum value allowed by the model<sup>17</sup>). We allowed the ionization parameters of both ionized absorbers and the redshift of the second ionized absorber to vary in the fit (model XSTAR3; Table 5). We find that the best fitted redshift of the second warm absorber is  $z \sim 2$  in both the FI and BI spectra. The  $F$ -test indicates an improvement in the fits of OBS1 with model XSTAR3, that assumes two ionized absorbers, compared to fits with models XSTAR1 and XSTAR2, that assume a single ionized absorber, at the  $\gtrsim 99.5\%$  of significance level in the FI and BI spectra. We conclude that a single warm-absorber model cannot accurately fit both the low and high-energy absorption in APM 08279+5255.

<sup>17</sup> The high-energy absorption features modeled with Gaussian absorption lines in model 7 could be the result of one or more highly ionized absorbers. The Doppler broadening velocities of each absorption line component of model 7 are  $\sim \frac{\sigma_{\text{abs}i}}{E_{\text{abs}i}}$  (where  $i=1,2$  indicates the component). From Table 3 these Doppler broadening velocities are at first order comparable to the assumed values of  $v_{\text{turb}}$ .

We finally assumed the spectral model XSTAR4 consisting of an absorbed power-law and two outflowing ionized absorbers. We assumed turbulent velocities of  $v_{\text{turb}} = 10,000 \text{ km s}^{-1}$  for the first and second outflowing ionized absorber (model XSTAR4; Table 5). The main difference between models XSTAR3 and XSTAR4 is that the redshift of the first warm-absorber is fixed in model XSTAR3 to the systemic redshift of the quasar and free to vary in model XSTAR4 and that model XSTAR4 includes a neutral absorber. For fits using model XSTAR4, we allow the redshifts, column densities, and ionization parameters of the absorbers to vary. The  $\chi^2$  values for these fits are similar to those found for model 7 (see Table 5 and 3). We find on average best-fit redshifts of  $z_{\text{abs}1} \sim 3$  ( $v_{\text{abs}1} \sim 0.2c$ ) and  $z_{\text{abs}2} \sim 2$  ( $v_{\text{abs}1} \sim 0.5c$ ), and column densities of  $\log N_{\text{H},\text{abs}1} \sim 23.0$  and  $\log N_{\text{H},\text{abs}2} \sim 23.2$ , where  $\text{abs}1$  and  $\text{abs}2$  correspond to the two warm absorbers. We confirm the results of model 7, by finding a significant change in the best-fitted redshift of the first warm-absorber component in model XSTAR4 between epochs OBS2 and OBS3 (see Table 5). Even though the two warm-absorber model results in acceptable fits, the best-fit parameters should only be con-

sidered as basic estimates of the wind properties since the kinematic and ionization structure of the outflow are likely to be more complicated. Our spectral fitting results of models that include ionized absorbers (see Table 5) indicate that both models XSTAR3 and XSTAR4 provide acceptable fits to the spectra of APM 08279+5255 for epochs OBS1 and OBS3, however, model XSTAR4 provides a better fit to the data for epoch OBS2 than model XSTAR3. The *F*-test indicates that in epoch OBS2, spectral fits using model XSTAR4 provide an improvement over fits using model XSTAR3 at the  $\sim 99\%$  level of significance in the FI and BI spectra.

### 3.2. PIN spectral analysis.

We also examined the spectrum of APM 08279+5255 in the 10–40 keV energy band using the PIN-HXD data. Unfortunately, no signal from the source above the background in the NXB was found. The background-subtracted source spectrum<sup>18</sup> was found to be within 5% of the non-X-ray background (NXB) spectrum provided by the *Suzaku* team (e.g., Mizuno et al. 2007). We arrive at a similar conclusion from the count rates presented in Table 2. The non-detection with the PIN provides an upper limit on the flux density at 20 keV of APM 08279+5255 of  $\sim 10^{-3}$  photons s $^{-1}$  keV $^{-1}$ . This limit is consistent with an extrapolation of the XIS spectrum.

## 4. DISCUSSION

The X-ray spectrum of APM 08279+5255 is known to contain absorption features at rest-frame energies above 7 keV (Chartas et al. 2002; Hasinger et al. 2002). These features have been interpreted in the past in two different ways. The first interpretation by Chartas et al. (2002) was based primarily on the analysis of the 2002 *Chandra* observation of APM 08279+5255 and posits that the absorption features are due to highly blueshifted Fe XXV K $\alpha$  and/or Fe XXVI K $\alpha$  absorption lines. An XMM-Newton observation of APM 08279+5255 performed 1.8 weeks (proper-time) after the *Chandra* observation showed significantly different high-energy absorption structure which was interpreted by Chartas et al. (2003) to imply variability of the absorption features over timescales of the order of weeks. The second interpretation by Hasinger et al. (2002) is based on the 2002 XMM-Newton observation of APM 08279+5255 and proposes that the high-energy absorption feature arises from an iron absorption edge produced by a metal enriched ( $\text{Fe}/\text{O} \approx 2-5 \text{ Fe}/\text{O}_{\odot}$ ) ionized absorber. One important conclusion from section 3.1.2 is that the absorption feature found at 7–12 keV rest-frame can be fitted with two highly ionized blue-shifted warm absorbers that do not require super-solar metallicities. We note that Hasinger et al. (2002) and Ramírez (2008) had claimed iron over-abundance ( $a_{\text{Fe}} > 2$ ) based on their analyses of previous observations of APM 08279+5255. In support of the two-component “iron-blend-outflow” scenario we mention that the two absorption-line model and the notch model (models 7 and 5; Table 3) provide significantly better fits to the absorption feature between

7–12 keV rest-frame than an absorption-edge model in epoch OBS1 (see §3). We also note that, in the 2002  $\sim 90$  ks *Chandra* observation analyzed in Chartas et al. (2002), the model containing two absorption lines successfully fits the 7–12 keV rest-frame feature whereas an absorption-edge model did not provide an acceptable fit. The absorption described either by two absorption lines or a notch, may crudely represent absorption through an outflow with a large velocity gradient along the flow. Variability of the kinematic and ionization state of the outflow may explain why, depending on the observation, these absorption features could be modelled by either a notch, absorption lines, or an edge (see figure 4 of Schurch & Done 2007). We conclude that a time-variable outflow provides a plausible explanation for all the past X-ray observations of the absorption features of APM 08279+5255 (Chartas et al. 2002; Hasinger et al. 2002) including those analyzed here. In §4.1 we provide plausible explanations for the observed variability of the high-energy absorption. In §4.2 we use the results of our spectral analysis to place constraints on the kinematics of the outflow and in §4.3 we provide estimates of the mass-outflow rate and efficiency of the outflow of APM 08279+5255.

### 4.1. Origin of the Variability of the High-Energy Absorption Feature.

Assuming the first interpretation of the origin of the high-energy absorption features in APM 08279+5255 the observed shift in the energy of the first absorption line between epochs OBS2 and OBS3 is likely due to a change in the outflow velocity of the absorber. Two alternative explanations of the shift are a change in the direction of the outflow (with respect to the line of sight) and a variation in the ionization parameter of the absorber. A change in the direction of the outflow is expected to show a shift in energy of both components of model 7 (Table 3). We only find variability in one component (abs1, see §3); however this picture could still be valid if each outflow component is driven independently. A change in the ionization parameter seems to be a less probable scenario. We checked this by fitting the spectra of epochs OBS2 and OBS3 simultaneously with model XSTAR4, keeping the redshift of abs1 as the only common parameter between the fits. In the case where a change in the ionization parameter produced the detected variability of the first absorption line abs1, we expect that the fits to the spectra of epochs OBS2 and OBS3 will not be improved by allowing the redshift of abs1 to vary independently in these fits. For the simultaneous fit to the spectra of epochs OBS2 and OBS3, where the redshift of abs1 was kept a common parameter, we find  $z_{\text{abs1}}(\text{FI}) = 3.11 \pm 0.04$ ,  $z_{\text{abs1}}(\text{BI}) = 3.04 \pm 0.06$ ,  $\chi^2_{\text{FI}}/\nu = 138.1/124$  and  $\chi^2_{\text{BI}}/\nu = 136.3/124$ . In the case where we fit the spectra of epochs OBS2 and OBS3 independently using model XSTAR4 (see Table 5) we find  $\chi^2_{\text{FI}}/\nu = 132.2/123$  and  $\chi^2_{\text{BI}}/\nu = 123.4/123$ .<sup>19</sup> The improvement based on the *F*-test of fitting the spectra of epochs OBS2 and OBS3 independently, compared to keeping a common redshift of abs1, is at the  $\sim 99\%$  and  $>99.9\%$  level of significance in the FI and BI spectra.

<sup>18</sup> The background-subtracted source spectrum is obtained by subtracting the non-X-ray-background and an estimate of the X-ray background from the total detected PIN spectrum

<sup>19</sup> These values are obtained by summing the  $\chi^2$  and degrees of freedom of epochs OBS2 and OBS3 in Table 5.

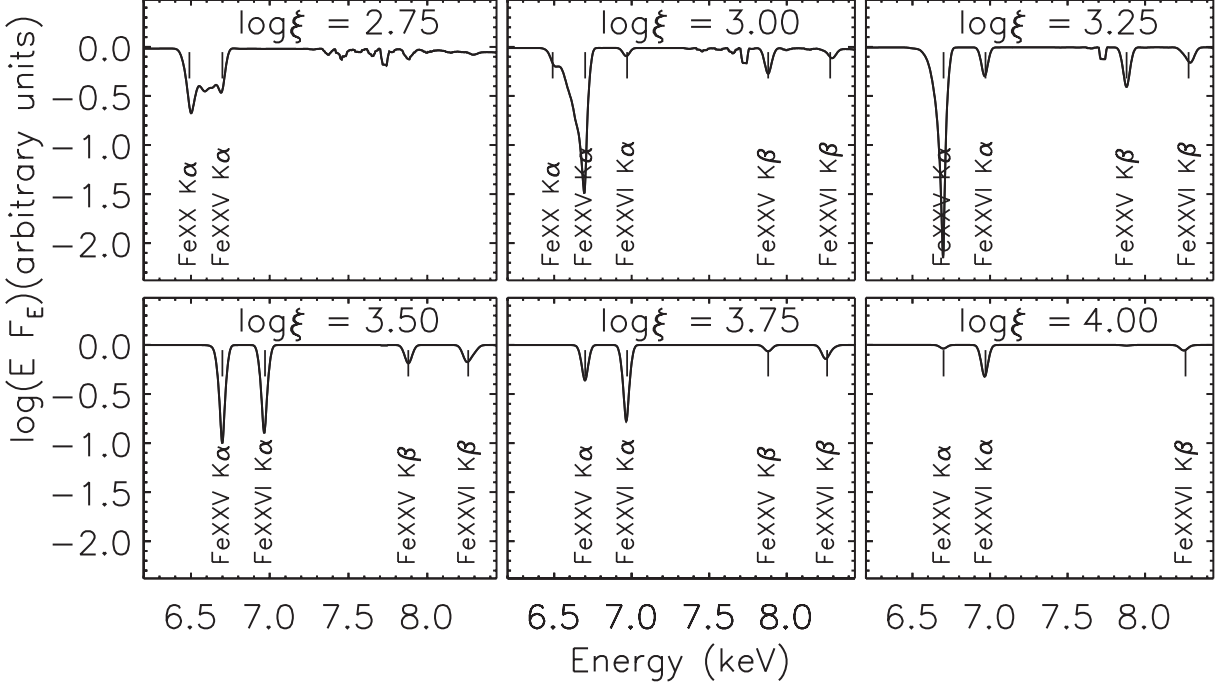


FIG. 3.— Simulated 6–8 keV absorbed spectra ( $\log(EF_E)$ ) assuming an incident power-law spectrum with a photon index of  $\Gamma=2$ . The ionized absorber is modeled with the XSTAR model WARMABS assuming a column density of  $\log N_{\text{H}} = 23$ , solar abundances,  $v_{\text{turb}} = 1000 \text{ km s}^{-1}$ , and the following six values of the ionization parameter  $\log \xi = 2.75, 3.00, 3.25, 3.50, 3.75$ , and  $4.0$ , respectively. Some of the main absorption lines in this range of ionization states have been marked in the figure. Among them Fe xx K $\alpha$  ( $2s^2 2p^3 - 1s2s^2 2p^4$ ; 6.50 keV), Fe xxv K $\alpha$  ( $1s^2 - 1s2p$ ; 6.70 keV), Fe xxv K $\beta$  ( $1s^2 - 1s3p$ ; 7.89 keV), Fe xxvi K $\alpha$  ( $1s - 2p$ ; 6.97 keV), Fe xxvi K $\beta$  ( $1s - 3p$ ; 8.27 keV).

We conclude that the variability of the energy of the first absorption line abs1 is likely not driven by changes in the ionization parameter of abs1. *Suzaku* cannot resolve the images of APM 08279+5255, however, the time-delays between the two brightest images A and B of APM 08279+5255 is estimated to be of the order of a few hours (e.g., Munoz et al. 2001), much shorter than the observed variability of the high-energy absorption feature. We therefore do not expect the combined X-ray spectrum of all images of APM 08279+5255 to differ from that of the individual images within the time-delay.

#### 4.2. Constraints on the Kinematics of the Outflow.

Under the premise of the outflow interpretation to explain the absorption at rest-frame 7–12 keV we expect a continuous distribution of outflow velocities. This range of velocities leads to the Doppler shift of the energies of the resonance absorption lines. The absorption-line rest-frame energies  $E_{\text{lab}}$  will thus be shifted to the observed energies  $E_{\text{obs}}$  according to

$$E_{\text{lab}}/E_{\text{obs}} = \gamma(1 - \beta \cos\theta), \quad (2)$$

where  $\gamma$  is the Lorentz factor,  $\theta$  is the angle between the wind and our line of sight (l.o.s), and  $\beta = v/c$ .

The minimum and maximum projected velocities ( $v_{\min}, v_{\max}$ ) of the outflow are estimated from the minimum and maximum energy ranges ( $E_{\min}, E_{\max}$ ) of the high-energy absorption features in APM 08279+5255. We obtained  $E_{\min}$  and  $E_{\max}$  from our spectral fits assuming first the two absorption-line (APL+2AL) model and second assuming the notch (APL+No) model. Specifically, based on the best-fit values of the APL+2AL model (model 7; Table 3), we obtain  $E_{\min} = E_{\text{abs1}} - 2\sigma_{\text{abs1}}$

and  $E_{\max} = E_{\text{abs2}} + 2\sigma_{\text{abs2}}$ . From the best-fit values of the APL+No model (model 5; Table 3) we have  $E_{\min} = E_{\text{notch}} - W_{\text{notch}}/2$  and  $E_{\max} = E_{\text{notch}} + W_{\text{notch}}/2$ . The values of  $E_{\min}$  and  $E_{\max}$  are presented in Table 6. In this table the values of  $E_{\min}$  and  $E_{\max}$  are shown separately for the FI and BI spectra and for the two different models used to obtain them (model 7≡APL+2AL; model 5≡APL+No).

The relative strengths of the iron resonance absorption lines will depend on the ionization state of the outflowing medium. To demonstrate this effect in a basic way we have performed several simulations using the warm-absorber model (WARMABS) of XSTAR. In Figure 3 we show a simulated absorbed spectrum in the 6–8 keV rest-frame energy range for an absorbing medium with solar composition,  $\log N_{\text{H}}=23$ , and having six different values of the ionization parameter ( $2.75 \lesssim \log \xi \lesssim 4.0$ ). The two strongest iron lines for this highly ionized absorbing medium have rest (or laboratory) energies of 6.70 keV (Fe xxv K $\alpha$ ;  $1s^2 - 1s2p$ ) and 6.97 keV (Fe xxvi K $\alpha$   $1s - 2p$ ). In general the Fe xxv K $\alpha$  line will be stronger than the Fe xxvi K $\alpha$  line for a medium with  $2.75 \lesssim \log \xi \lesssim 4.0$ . Therefore the absorption at the lower end of the 7–12 keV rest-frame range is most likely associated with the Fe xxv K $\alpha$  line. Based on our interpretation of the high-energy absorption features we estimate  $v_{\min}$  assuming that the absorption at the low end of the X-ray BAL is due to a line arising from highly blueshifted Fe xxv K $\alpha$  ( $E_{\text{lab}} = 6.7$  keV). On the other hand to estimate  $v_{\max}$  we make the conservative assumption that the absorption at the high end of the X-ray BAL is due to a line arising from highly blueshifted Fe xxvi K $\alpha$  ( $E_{\text{lab}} = 6.97$  keV). The estimated values of  $v_{\min}$  and  $v_{\max}$  obtained through the procedure outlined above are

TABLE 6  
THE MINIMUM AND MAXIMUM ENERGIES AND VELOCITIES OF THE HIGH-ENERGY ABSORPTION FEATURES IN APM 08279+5255.

Model <sup>a</sup>	OBS	Instrument	$E_{\min}$ [keV]	$E_{\max}$ [keV]	$v_{\min}$ [c]	$v_{\max}$ [c]
5.....	1	XIS FI	7.60±0.24	11.58±0.24	0.13±0.03	0.52±0.02
7.....	1	XIS FI	7.52±0.36	12.16±0.52	0.12±0.05	0.56±0.04
5.....	2	XIS FI	7.82±0.37	11.68±0.37	0.16±0.05	0.52±0.03
7.....	2	XIS FI	7.88±0.48	11.57±0.51	0.17±0.06	0.51±0.04
5.....	3	XIS FI	7.38±0.34	11.42±0.34	0.10±0.05	0.50±0.03
7.....	3	XIS FI	7.51±0.32	11.70±1.06	0.12±0.05	0.52±0.08
5.....	1	XIS BI	7.46±0.53	12.17±0.53	0.11±0.08	0.56±0.04
7.....	1	XIS BI	7.24±0.51	12.47±1.12	0.08±0.07	0.58±0.08
5.....	2	XIS BI	7.91±0.78	12.92±0.78	0.18±0.10	0.61±0.05
7.....	2	XIS BI	8.74±0.58	12.24±1.16	0.28±0.07	0.56±0.08
5.....	3	XIS BI	7.70±0.63	12.22±0.63	0.15±0.09	0.56±0.04
7.....	3	XIS BI	7.53±0.82	12.40±0.92	0.12±0.11	0.57±0.06
7.....	Cha02 <sup>b</sup>	ACIS BI	7.95±0.11	10.28±0.22	0.18±0.01	0.40±0.02
7.....	Has02 <sup>b</sup>	EPIC pn	6.95±0.44	15.00±1.06	<0.10	0.72±0.05

<sup>a</sup> Model used to estimate  $E_{\min}$  and  $E_{\max}$ . Model 5 (see Table 3) is a power-law with Galactic absorption, intrinsic absorption, and a notch absorber; Model 7 (see Table 3) is a power-law with Galactic absorption, intrinsic absorption, and two absorption lines.<sup>b</sup> In this Table we identify as Cha02 the 88.8 ks observation of APM 08279+5255 performed with *Chandra* in 2002 and analyzed in detail in Chartas et al. (2002). We also identify as Has02 the 100.2 ks observation of APM 08279+5255 performed with *XMM-Newton* in 2002 and analyzed in detail in Hasinger et al. (2002).

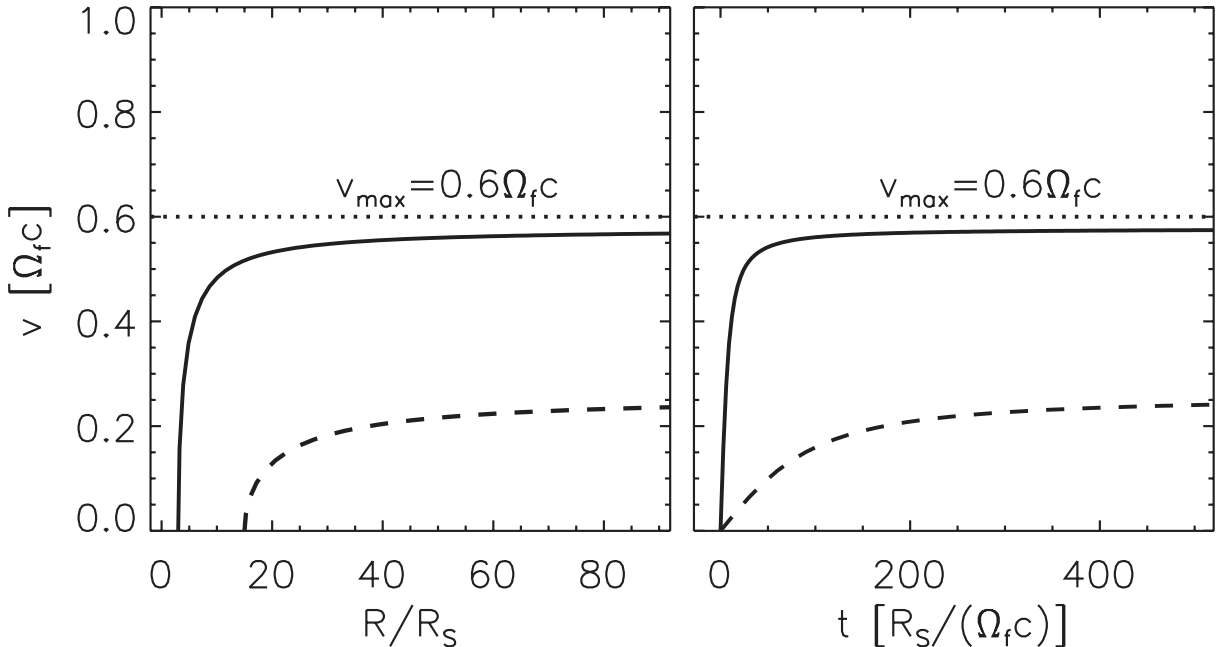


FIG. 4.— Wind velocity (in units of  $\Omega_f c$ ) plotted as a function of radius from the central source (left panel) and as a function of time (right panel) for a radiation-pressure driven wind. Notice that the radius is in units of the Schwarzschild radius ( $R_S = \frac{2GM}{c^2}$ ) and the time is in units of  $\tau = \frac{R_S}{\Omega_f c}$ . The wind velocities are calculated for  $R_{\text{launch}} = 3R_S$  and  $R_{\text{launch}} = 15R_S$ , respectively.

presented in Table 6. These velocities are obtained using equation (2) assuming that our line-of-sight makes an angle of  $\theta = 20^\circ$  with the velocity of the outflow (Chartas et al. 2007a). A change of  $10^\circ$  in  $\theta$  will introduce a variation of  $\lesssim 10\%$  in our estimates of the velocities. The velocities of the outflow range between  $0.1c$  and  $0.6c$ . The mean value of  $E_{\max}$  from all CCDs and observations is  $12.04 \pm 0.22$  keV corresponding to a mean value of  $v_{\max} = 0.55 \pm 0.02c$ . This maximum value of the outflow velocity constrains the angle between the outflow

direction and our line of sight to be  $< 36^\circ$ .<sup>20</sup> This relatively small angle is consistent with outflow models that posit that BAL quasars are viewed through collimated outflows.

As argued in Chartas et al. (2002, 2003, 2007a) we are likely observing the X-ray absorbers as they are accel-

<sup>20</sup> The Doppler-shift formula (equation 2) predicts that given a fixed ratio of  $E_{\text{lab}}/E_{\text{obs}} \equiv R_{lo}$  the maximum angle between our line of sight and the wind direction is given by  $\theta_{\max} = \cos^{-1}(\sqrt{1 - R_{lo}^2})$ .

erated near their launching radii. We use the following equation to describe the basic dynamics of a radiation-driven outflow (e.g., equation 1 of Chartas et al. 2002):

$$v_{\text{wind}} = [(\Gamma_f \frac{L_{\text{UV}}}{L_{\text{Edd}}} - 1) (\frac{1}{R_{\text{launch}}} - \frac{1}{R})]^{1/2} \quad (3)$$

where  $v_{\text{wind}}$  is the outflow velocity in units of  $c$ ,  $\Gamma_f$  is the force multiplier,  $L_{\text{Edd}}$  is the Eddington luminosity,  $R_{\text{launch}}$  is the radius (units of  $R_S$ ) at which the wind is launched from the disk, and  $R$  is the distance (units of  $R_S$ ) from the central source. The expression for the dynamics of the outflow can be simplified by defining

$$\Omega_f = \sqrt{\Gamma_f \frac{L_{\text{UV}}}{L_{\text{Edd}}} - 1}.$$

In Figure 4 we plot wind velocity versus radius (left panel) and wind velocity versus time (right panel) for an outflow launched at radii of  $3R_S$  (solid lines) and  $15R_S$  (dashed lines). In Figure 4 the units of velocity, distance, and time are  $\Omega_f c$ ,  $R_S$ , and  $R_S/(\Omega_f c)$ , respectively. Assuming  $L_{\text{UV}} \sim 0.2 L_{\text{bol}}$  (Irwin et al. 1998),  $L_{\text{bol}}/L_{\text{Edd}} \sim 0.2$  and  $\Gamma_f \sim 100$  (e.g., Arav et al. 1994; Laor & Brandt 2002), we have  $\Omega_f \sim 1.7$ .  $L_{\text{bol}}/L_{\text{Edd}} \sim 0.2$  is obtained using the  $L_{\text{bol}}/L_{\text{Edd}}$  vs.  $\Gamma$  correlation found in RQ quasars (e.g., Wang et al. 2004; Shemmer et al. 2006, 2008) for  $\Gamma \sim 1.9$ . Therefore with  $L_{\text{bol}} = 7 \times 10^{15} \mu_L^{-1} L_\odot$  (Irwin et al. 1998; Reichers et al. 2008)<sup>21</sup>  $M_{\text{BH}} \sim 10^{12} M_\odot \mu_L^{-1}$ , where  $\mu_L \sim 100$  (Egami et al. 2000)<sup>22</sup> is the lens magnification factor. Equation 3 could be modified using a reliable SED describing the central source, adding relativistic corrections, and calculating the force multiplier at every point of the trajectory of the outflow. We stress, however, that our simplified approach is sufficient to provide first order approximations to the launching radius and the time scales involved in the dynamics of the outflow. Equation 3 can be written as  $R_{\text{launch}}/R_S = \Omega_f^2 (c/v_\infty)^2$ ; therefore for  $\Omega_f \sim 1.7$   $R_{\text{launch}} \sim 3 \times (c/v_\infty)^2 R_S$ . The latter expression can be used to obtain first order approximations of the launching radius given the velocity of the outflow.

Assuming a radiation-driven wind, it is expected that the time required to accelerate the outflow to fractions of  $c$  is of the order of  $10 \frac{R_S}{c}$  (see Figure 4). For the black-hole mass of APM 08279+5255 of  $M_{\text{BH}} \approx 10^{10} M_\odot$  we estimate that the time to accelerate an absorber to near-relativistic velocities is  $\sim$ weeks (rest-frame). We have reported in this work probable variability of the high-energy absorption features over a time-scale of  $\sim$ 1 month (rest-frame). This short time-scale variability is consistent with the expected variability timescale of a radiation-driven wind.

#### 4.3. Constraints on Mass-Outflow Rate and Efficiency of the Outflow.

Based on our estimated values of the outflow velocities, column densities, and launching radii we present constraints on the mass-outflow rates and outflow efficiency associated with the outflowing X-ray absorbers of

<sup>21</sup> We note that an estimation of  $L_{\text{bol}}$  based on the optical and UV spectra should be more precise than an extrapolation of  $L_{\text{bol}}$  based on X-ray luminosities as it is done in Ramírez (2008).

<sup>22</sup> See, however, Reichers et al. (2008) that find a magnification of  $\mu_L \sim 4$ . Reichers et al. (2008) also use the observed width of the CIV line to obtain a black-hole mass of  $M_{\text{BH}} \sim 10^{11} \mu_L^{-1} M_\odot$

APM 08279+5255. The efficiency is defined as the ratio of the rate of kinetic energy injected into the ISM and IGM by the outflow to the quasar's bolometric luminosity, i.e.,

$$\epsilon_K = \frac{1}{2} \frac{\dot{M} v^2}{L_{\text{bol}}}, \text{ where } \dot{M} = 4\pi R^2 \rho v f_c = 4\pi f_c \frac{R^2}{\Delta R} N_{\text{H}} m_p v, \quad (4)$$

where  $f_c$  is the covering fraction,  $N_{\text{H}}$  is the column density,  $R$  is the radius, and  $\Delta R$  is the thickness of the absorber. To estimate the efficiency we use the two absorption-line model (APL+2AL; model 7 of Table 3). We calculate the bulk velocities of each outflow component based on the energies of the absorption lines in model 7 and through the use of equation (2) with  $E_{\text{lab}}=6.7$  keV and  $\theta = 20^\circ$ . As in Chartas et al. (2002, 2003) we interpret the high-energy absorption features as being due to highly ionized Fe (Fe xxv K $\alpha$ ) in a gas with solar abundances, and we estimate  $\log N_{\text{H}}$  using a curve-of-growth analysis. In Table 7 we present the outflow velocities,  $v_{\text{abs}}$ , the column densities,  $\log N_{\text{H}}$ , the mass-outflow rates,  $\dot{M}$ , and the outflow efficiencies,  $\epsilon_K$ , of the two modeled absorbers of the outflow. We note that the values of the column densities and velocities in Table 7 are consistent with those found using the photoionization code XSTAR (see Table 5).<sup>23</sup>

To obtain error bars for  $\epsilon_K$  and  $\dot{M}$  we performed a Monte Carlo simulation, assuming a uniform distribution of the parameters  $f_c$ ,  $R$  and  $R/\Delta R$  around the expected values of these parameters, and a normal distribution for  $\log N_{\text{H}}$  (described by the parameters in Table 7). Specifically, we assume a covering factor lying in the range  $f_c = 0.1 - 0.3$ , based on the observed fraction of BAL quasars (e.g., Hewett & Foltz 2003) and a fraction  $R/\Delta R$  ranging from 1 to 10 based on current theoretical models of quasar outflows (e.g., Proga et al. 2000). Note that in Table 7 we also include the outflow parameters of the  $\sim$ 90 ks *Chandra* observation of APM 08279+5255 performed in 2002 (Chartas et al. 2002). Based on our estimated maximum outflow velocities ( $v_{\text{max}} \sim 0.6c$ ) we expect that  $R$  will be similar to  $R_{\text{launch}}$  and range between  $3R_S$  and  $15R_S$  (see Figure 4). We note that this is a conservative assumption since larger values of  $R$  will result in larger mass-outflow rates and larger efficiencies. Additionally, the short variability time-scales ( $\sim$ weeks) are also consistent with a launching radius of a few times  $R_S$ . Variability in APM 08279+5255 over time-scales  $\sim$ weeks has been previously reported (Chartas et al. 2003) based on the differences of the high-energy absorption features detected in the *Chandra* and *XMM-Newton* observations. Our current analysis of the *Suzaku* observations of APM 08279+5255 allows us to compare absorption features observed with the same instruments; therefore, it avoids any possible systematic uncertainties due to differences in the responses of the instruments.

Our results indicate that the average fraction of the total bolometric luminosity of APM 08279+5255 injected into the IGM in the form of kinetic energy is  $\epsilon_K = 0.7 \pm 0.3$ . From the results of Table 7 we also obtain the aver-

<sup>23</sup> The velocities obtained in Table 5 assume the redshifts of the absorbers in model XSTAR4 are due to the relativistic Doppler effect (see equation 2).

TABLE 7  
PROJECTED MAXIMUM OUTFLOW VELOCITIES, MASS-OUTFLOW RATES AND EFFICIENCIES OF OUTFLOWS IN APM 08279+5255 <sup>a</sup>.

OBS	Instr.	$v_{\text{abs}1}$ [c]	$\log N_{\text{H}}(\text{abs}1)$	$\dot{M}$ (abs1) [ $M_{\odot}\mu_L^{-1}\text{yr}^{-1}$ ]	$\epsilon_K$ (abs1)	$v_{\text{abs}2}$ [c]	$\log N_{\text{H}}(\text{abs}2)$	$\dot{M}$ (abs2) [ $M_{\odot}\mu_L^{-1}\text{yr}^{-1}$ ]	$\epsilon_K$ (abs2)
1	XIS FI	$0.20^{+0.01}_{-0.02}$	$22.84 \pm 0.19$	$470^{+478}_{-319}$	$0.02^{+0.02}_{-0.01}$	$0.47^{+0.02}_{-0.03}$	$23.07 \pm 0.27$	$2072^{+2388}_{-1496}$	$0.5^{+0.6}_{-0.4}$
2	XIS FI	$0.27^{+0.03}_{-0.02}$	$22.86 \pm 0.25$	$713^{+794}_{-507}$	$0.05^{+0.06}_{-0.04}$	$0.49^{+0.02}_{-0.02}$	$22.81 \pm 0.39$	$1468^{+2071}_{-1167}$	$0.4^{+0.5}_{-0.3}$
3	XIS FI	$0.17^{+0.01}_{-0.01}$	$22.87 \pm 0.28$	$479^{+561}_{-350}$	$0.01^{+0.02}_{-0.01}$	$0.44^{+0.04}_{-0.04}$	$23.05 \pm 0.19$	$1678^{+1707}_{-1141}$	$0.3^{+0.4}_{-0.2}$
1	XIS BI	$0.17^{+0.03}_{-0.02}$	$22.89 \pm 0.24$	$475^{+520}_{-333}$	$0.01^{+0.02}_{-0.01}$	$0.46^{+0.03}_{-0.03}$	$23.48 \pm 0.20$	$4772^{+4912}_{-3266}$	$1.1^{+1.1}_{-0.2}$
2	XIS BI	$0.34^{+0.02}_{-0.03}$	$23.01 \pm 0.36$	$1520^{+2040}_{-1179}$	$0.19^{+0.25}_{-0.15}$	$0.53^{+0.05}_{-0.07}$	$23.09 \pm 0.36$	$2849^{+3822}_{-2210}$	$0.8^{+1.1}_{-0.7}$
3	XIS BI	$0.22^{+0.04}_{-0.05}$	$23.10 \pm 0.21$	$962^{+1006}_{-663}$	$0.05^{+0.05}_{-0.03}$	$0.50^{+0.04}_{-0.04}$	$23.14 \pm 0.24$	$2486^{+2722}_{-1753}$	$0.7^{+0.7}_{-0.5}$
Ch02	ACIS BI	$0.20^{+0.01}_{-0.01}$	$22.99 \pm 0.11$	$622^{+570}_{-420}$	$0.03^{+0.02}_{-0.02}$	$0.40^{+0.01}_{-0.01}$	$23.07 \pm 0.12$	$1507^{+1398}_{-979}$	$0.3^{+0.2}_{-0.2}$
Has02	EPIC pn	$0.21^{+0.03}_{-0.03}$	$23.10 \pm 0.36$	$1155^{+1550}_{-896}$	$0.10^{+0.14}_{-0.08}$	$0.50^{+0.06}_{-0.07}$	$23.36 \pm 0.30$	$4500^{+5443}_{-3329}$	$1.2^{+1.4}_{-0.9}$

<sup>a</sup> The estimated values of the outflow properties were based on fits that assumed an absorbed power-law model with two absorption lines. The values of  $\dot{M}$  and  $\epsilon_K$  are obtained by equation (4) assuming  $M_{\text{BH}} \sim 10^{12}\mu_L^{-1}M_{\odot}$  (see §4.2) and  $L_{\text{bol}} = 7 \times 10^{15}\mu_L^{-1}L_{\odot}$  (Irwin et al. 1998; Reichers et al. 2008).

age mass-outflow rate of  $\dot{M} = 3324 \pm 915 \mu_L^{-1}M_{\odot}\text{yr}^{-1}$ . On the other hand the mass-accretion rate is  $\dot{M}_{\text{acc}} = \frac{L}{\eta c^2} \sim 4840\mu_L^{-1}M_{\odot}\text{yr}^{-1}$  (assuming  $\eta \approx 0.1$  and  $L_{\text{bol}} = 7 \times 10^{15}\mu_L^{-1}L_{\odot}$ ). Therefore the mass-outflow rate is comparable to the accretion rate. In the context of recent models of structure formation (e.g., Granato et al. 2004; Springel et al. 2005), our estimated values of  $\epsilon_K$  in APM 08279+5255 suggest that these outflows should be an important source of feedback in their host galaxies and also play an important role in regulating the growth of the central black hole.

To obtain an independent estimate of the mass-outflow rate  $\dot{M}$ , we derive  $nR^2$  based on the definition of  $\xi = L/(nR^2)$ . Assuming  $\log \xi \sim 3.5$  (e.g., model XSTAR4, Table 5) and an ionizing luminosity similar to the X-ray luminosity  $L_X \sim 4 \times 10^{46}\mu_L^{-1}\text{erg s}^{-1}$ , we obtain  $nR^2 \sim 1 \times 10^{43}\mu_L^{-1}\text{cm}^{-1}$ . Therefore assuming an overall velocity of the outflow  $\sim 0.45c$  we find  $\dot{M} \sim 9 \times 10^3\mu_L^{-1}M_{\odot}\text{yr}^{-1}$ . The value of  $\dot{M}$  derived from the best-fit ionization parameter is comparable (within a factor of three) to the value found for the second absorber abs2 in Table 7, where we have estimated the location of the absorber from variability arguments. We caution, however, that the estimation of the mass-outflow rate from the ionization parameter assumes a spherical outflow illuminated by a point source. However, since we expect that the X-ray absorber is located a few  $r_g$  from the X-ray source the point source approximation may not be accurate in this case.

## 5. CONCLUSIONS

Our analysis of three long *Suzaku* observations of the BAL quasar APM 08279+5255 indicates strong and broad absorption at rest-frame energies of  $\lesssim 2$  keV (low-energy) and 7–12 keV (high-energy). Based on the *F*-test the low-energy absorption is significant at the  $\gtrsim 99\%$  and  $\gtrsim 99.9\%$  levels in the front-illuminated (FI) and back-illuminated (BI) *Suzaku* XIS spectra, respectively. The high-energy absorption is significant at  $\gtrsim 99.9\%$  (FI spectrum) and at  $\gtrsim 99\%$  (BI spectrum) confidence, respectively. The medium producing the low-energy absorption is a nearly neutral absorber with a column density  $\log N_{\text{H}} \sim 23$ . The medium producing the high-energy absorption appears to be outflowing from the central source at near-relativistic velocities and with

large ionization parameters ( $2.75 \lesssim \log \xi \lesssim 4.0$ ), consistent with results obtained from a previous *Chandra* observation of this object (Chartas et al. 2002). Simulations of highly ionized near-relativistic winds performed by Schurch & Done (2007) indicate that the resulting X-ray broad absorption profile may have the apparent shape of an absorption edge, a notch, or a combination of absorption lines depending on the assumed dynamics and degree of ionization of the outflowing absorbers.

Our observations of the 7–12 keV rest-frame features are well described by a two component absorber model. We find that in epoch OBS1, spectral fits with the two component absorption-line model (APL + 2AL) are significantly better ( $> 95\%$  confidence level) than fits with absorption-edge models (APL + Ed). We note that spectral fits with models that included ionized absorbers with free iron abundances (models XSTAR2 and XSTAR3 in Table 5) are consistent with no iron over-abundance in all *Suzaku* observations of APM 08279+5255.

Our interpretation, of a near-relativistic outflowing absorbing medium in a high ionization state ( $2.75 \lesssim \log \xi \lesssim 4$ ), is consistent with our analysis of all the past X-ray observations of APM 08279+5255. Our spectral analysis indicates that the outflow velocities of the highly ionized absorbers detected in the three *Suzaku* observations range between  $0.1c$  and  $0.6c$ . The maximum detected projected outflow velocity of  $\sim 0.6c$  constrains the angle between our line of sight and the wind direction to be  $\lesssim 36^\circ$ . We find possible variability of the high-energy absorption lines between epochs OBS2 and OBS3 at the  $\sim 99.9\%$  and  $\sim 98\%$  significance levels in the FI and BI spectra, respectively. Our spectral analysis indicates that the variability is likely due to a change in the outflow velocity of the absorber. The short time-scale ( $\sim$ month in the rest-frame) of this variability is probably indicating that this absorber is strongly accelerated. This short time-scale variability combined with the high ionization of the absorbing material imply that the absorbers are launched from distances  $\lesssim 10R_S$  from the central source.

Assuming our interpretation that the absorption lines detected at rest-frame energies of 7–12 keV are due to Fe xxv, we estimate that a significant fraction ( $0.7 \pm 0.3$ ) of the total bolometric energy over the quasar's lifetime is injected into the intergalactic medium of APM 08279+5255 in the form of kinetic energy with a mass-outflow rate of  $\dot{M} = 3324 \pm 915 \mu_L^{-1}M_{\odot}\text{yr}^{-1}$ .

We would like to thank Michael Eracleous and Konstantin Getman for helpful discussions related to spectral models and statistical tests implemented in this

work. We acknowledge financial support by NASA grant NNX08AZ67G and NASA LTSA grant NAG5-13035.

## REFERENCES

- Arav, N., Li, Z., & Begelman, M.C. 1994, *ApJ*, 432, 62.
- Bahcall, N. A., & Fan, X. 1998, *ApJ*, 504, 1.
- Begelman, M. C., McKee, C. F., & Shields, G. A. 1983, *ApJ*, 271, 70.
- Best, P. N., Kauffmann, G., Heckman, T. M., Brinchmann, J., Charlot, S., Ivezić, Ž., & White, S. D. M. 2005, *MNRAS*, 362, 25.
- Boldt, E. 1987, *IAUS*, 124, 611.
- Blundell, K. M., Beasley, A.J., Lacy, M., & Garrington, S.T. 1996, *ApJ*, 468, L91.
- Chartas, G., Brandt, W. N., Gallagher, S. C., & Proga, D. 2007a, *AJ*, 133, 1849.
- Chartas, G., Eracleous, M., Dai, X., Agol, E., & Gallagher, S. 2007b, *ApJ*, 661, 678.
- Chartas, G., Brandt, W. N., & Gallagher, S. C. 2003, *ApJ*, 595, 85.
- Chartas, G., Brandt, W. N., Gallagher, S. C., & Garmire, G. P. 2002, *ApJ*, 579, 169.
- Chartas, G. 2000, *ApJ*, 531, 81.
- Chelouche, D. & Netzer, H. 2003, *MNRAS* 344, 233.
- Dadina, M. & Cappi, M. 2004, *A&A*, 413, 921.
- Dai, X., Shankar, F., & Sivakoff, G.R. 2008 *ApJ*, 672, 108.
- Downes D., Neri R., Wiklind T., Wilner D.J., & Shaver P.A. 1999, *ApJ* 513, L1
- Egami, E., Neugebauer, G., Soifer, B.T., Matthews, K., Ressler, M., Becklin, E. E., Murphy, T.W., Jr., & Dale, D.A. 2000, *ApJ*, 535, 561.
- Elvis, M. 2000, *ApJ*, 545, 63.
- Everett, J. E. 2005, *ApJ*, 631, 689.
- Everett, J. E. 2007, *Ap&SS*, 311, 269.
- Fabian, A. C. 1999, *MNRAS*, 308, 39.
- Fabian, A.C., Sanders, J.S., Ettori, S., Taylor, G.B., Allen, S.W., Crawford, C.S., Iwasawa, K., Johnstone, R.M., & Ogle, P.M. 2000, *MNRAS*, 318L, 65.
- Fabian, A.C., Vasudevan, R.V., & Gandhi, P. 2008, *MNRAS*, 385, 43.
- Ferrarese, L., & Merritt, D. 2000, *ApJ*, 539, 9.
- Gallagher, S. C., Brandt, W. N., Sambruna, R. M., Mathur, S., & Yamasaki, N. 1999, *ApJ*, 519, 549.
- Gallagher, S. C., Brandt, W.N., Chartas, G., & Garmire, G. P. 2002, *ApJ*, 567, 37.
- Gallagher, S.C., Brandt, W.N., Chartas, G., Priddey, R., Garmire, G.P., & Sambruna, R.M. 2006, *ApJ*, 644, 709.
- Gallimore, J.F., Axon, D.J., O'Dea, C.P., Baum, S.A., & Pedlar, A., 2006, *AJ*, 132, 546.
- Gebhardt, K., Kormendy, J., Ho, L.C., Bender, R., Bower, G., Dressler, A., Faber, S.M., Filippenko, A.V., Green, R., Grillmair, C., Lauer, T.R., Magorrian, J., Pinkney, J., Richstone, D., & Tremaine, S. 2000, *ApJ*, 543, 5
- Giustini, M., Cappi, M., Vignali, C. 2008, *A&A*, 491, 425
- Gibson, Robert R., Brandt, W. N., Schneider, Donald P., & Gallagher, S. C. 2008, *ApJ*, 675, 985.
- Granato, G.L., De Zotti, G., Silva, L., Bressan, A., & Danese, L. 2004, *ApJ*, 600, 580.
- Green, P.J. & Mathur, S. 1996, *ApJ*, 462, 637.
- Hasinger, G., Schartel, N., & Komossa, S. 2002, *ApJ*, 573, L77.
- Heinz, S., Choi, Y., Reynolds, C.S., & Begelman, M.C. 2002, *ApJ*, 569, L79.
- Hewett, P.C. & Foltz, C.B. 2003, *AJ*, 125, 1784.
- Hilton, M., Collins, C.A., Stanford, S.A., Lidman, C., Dawson, K.S., Davidson, M., Kay, S.T., Liddle, A.R., Mann, R.G., Miller, C.J., Nichol, R.C., Romer, A.K., Sabirli, K., Viana, P.T.P., & West, M.J. 2007, *ApJ* 670, 1000.
- Hopkins, P.F., Hernquist, L., Cox, T.J., Di Matteo, T., Robertson, & B., Springel, V. 2005, *ApJ*, 632, 81.
- Irwin, M.J., Ibata, R.A., Lewis, G.F., & Totten, E.J. 1998, *ApJ*, 505, 529.
- Jiang, L., Fan, X., Ivezić, Ž., Richards, G.T., Schneider, D.P., Strauss, M.A., & Kelly, B.C. 2007, *ApJ*, 656, 680.
- Kalberla, P.M.W., Burton, W.B., Hartmann, D., Arnal, E.M., Bajaja, E., Morras, R., & Pöppel, W. G. L. 2005, *A&A*, 440, 775.
- Kallman, T. R., Liedahl, D., Osterheld, A., Goldstein, & W., Kahn, S. 1996, *ApJ*, 465, 994.
- Kallman, T., & Bautista, M. 2001, *ApJS*, 133, 221.
- Krolik, J. H., & Begelman, M. C., 1986, *ApJ*, 308, L55.
- La Franca, F., Gregorini, L., Cristiani, S., de Ruiter, H., & Owen, F. 1994, *AJ*, 108, 1548.
- Laor, A., & Brandt, N. 2002, *ApJ*, 569, 641.
- McNamara, B.R., Wise, M., Nulsen, P.E.J., David, L. P., Sarazin, C.L., Bautz, M., Markevitch, M., Vikhlinin, A., Forman, W.R., Jones, C., & Harris, D.E. 2000, *ApJ*, 534L, 135.
- McNamara, B. R., & Nulsen, P. E. J. 2007, *ARA&A*, 45, 117.
- Mizuno, T., Takahashi, H., Uehara, Y., Nakazawa, K., Bamba, A., Fukasawa, Y., Kokubun, M., & Watanabe, S. 2007, *JX-ISAS-SUZAKU-MEMO-2007-09*.
- Muñoz, J. A., Kochanek, C. S., & Keeton, C. R. 2001, *ApJ*, 558, 657.
- Murray, N., Chiang, J., Grossman, S. A., & Voit, G. M. 1995, *ApJ*, 451, 498.
- Peacock, J.A., Miller, L., & Longair, M. S. 1986, *MNRAS*, 218, 265
- Pounds, K.A., King, A.R., Page, K.L., & O'Brien, P.T. 2003, *MNRAS*, 346, 1025.
- Proga, D., Stone, J.M., & Kallman, T.R. 2000, *ApJ*, 543, 686.
- Protassov, R., van Dyk, D. A., Connors, A., Kashyap, V. L., Siemiginowska, A. 2002, *ApJ*, 571, 545.
- Ramírez, J. M. 2008, *A&A*, 489, 57.
- Reeves, J.N., O'Brien, P.T., & Ward, M.J. 2003, *ApJ*, 593L, 65.
- Riechers, D.A., Walter, F., Carilli, C.L., & Lewis, G.F.
- Schindler, S., Castillo-Morales, A., De Filippis, E., Schwone, A. & Wambsganss, J. 2001, *A&A*, 376, L27.
- Schneider, D.P., van Gorkom, J.H., Schmidt, M., & Gunn, J. E. 1992, *AJ*, 103, 1451.
- Schurch, N. J., & Done, C. 2007, *MNRAS*, 381, 1413.
- Shemmer, O., Brandt, W.N., Netzer, H., Maiolino, R., & Kaspi, S. 2006, *ApJ*, 646, L29.
- Shemmer, O., Brandt, W.N., Netzer, H., Maiolino, R., & Kaspi, S. 2008, *ApJ*, 682, 81.
- Springel, V., Di Matteo, T., & Hernquist, L. 2005, *ApJ*, 620, L79.
- Srianand, R. & Petitjean, P. 2000, *A&A*, 357, 414.
- Vaughan S., & Uttley P. 2008, *MNRAS*, 390, 421.
- Wang, J., Watarai, K., & Mineshige, S. 2004, *ApJ*, 607, L107.
- Weymann, R.J., Morris, S.L., Foltz, C.B., & Hewett, P.C. 1991, *ApJ*, 373, 23.
- Younger, J.D., Bahcall, N.A., & Bode, P. 2005, *ApJ*, 622, 1
- Zheng, Z. Y., & Wang, J. X. 2008, *ApJ*, 688, 116
- Zhou, H., Wang, T., Wang, H., Wang, J., Yuan, W., & Lu, Y. 2006, *ApJ*, 639, 716.